bioRxiv preprint doi: https://doi.org/10.64898/2026.04.09.717438; this version posted April 12, 2026. The copyright holder for this preprint (which was not certified by peer review) is the author/funder, who has granted bioRxiv a license to display the preprint in perpetuity. It is made available under a CC-BY 4.0 International license.

The compartmentalized activity of a legume subtilase SBT12a allows symbiosome stabilization

Guofeng Zhang[1], Fabian Stockert[1,5], Melissa Mantz[1], Marta Rodriguez-Franco[1], Fabian van Beveren[2], Casandra Hernández-Reyes[1,6], Beatrice Lace[1], Wei Yang[3], Hector Mancilla[4], Aida Maric[1,6], Nils Nebel[1], Sjon Hartman[1,6], Claudine Kraft[4,6], Chao Su[3], Pierre-Marc Delaux[2], Pitter F. Huesgen[1,6] and Thomas Ott[1,6*]

Affiliations

[1] Faculty of Biology, University of Freiburg, 79104 Freiburg, Germany

[2] Laboratoire de Recherche en Sciences Végétales (LRSV), Université de Toulouse, CNRS, Toulouse INP, Castanet-Tolosan, France

[3] Hubei Hongshan Laboratory, National Key Laboratory of Crop Genetic Improvement, College of Plant Science and Technology, Huazhong Agricultural University, Wuhan, China

[4] Institute of Biochemistry and Molecular Biology, ZBMZ, Faculty of Medicine, University of Freiburg, 79104 Freiburg, Germany

[5] Spemann Graduate School of Biology and Medicine (SGBM), University of Freiburg, 79104 Freiburg, Germany

[6] CIBSS – Centre for Integrative Biological Signalling Studies, University of Freiburg; 79104 Freiburg, Germany

Corresponding author: Ott, Thomas (ott@bio.uni-freiburg.de)

Abstract

The stabilization of rhizobia in specialized organelles, called symbiosomes, is an evolutionary hallmark for maintaining high rates of nitrogen fixation in legumes. This is achieved by releasing thousands of bacteria from nodular infection threads within in a single plant cell, which poses a great challenge for the host to keep control over these differentiated bacteria. Considering the

bioRxiv preprint doi: https://doi.org/10.64898/2026.04.09.717438; this version posted April 12, 2026. The copyright holder for this preprint (which was not certified by peer review) is the author/funder, who has granted bioRxiv a license to display the preprint in perpetuity. It is made available under a CC-BY 4.0 International license.

importance of proteolytic degradation of antimicrobial proteins or generation of symbiosis-promoting peptides, proteolytic activity may represent a key regulatory system. Indeed, we identified the *Medicago truncatula* subtilisin-like protease (subtilase, SBT) 12a acting as a novel regulator of symbiosome functionality and maintenance. Loss-of-function mutations in *SBT12a* led to severe symbiotic defects with nodules of *sbt12a* being characterized by high level induction of defense/senescence-related genes. Using untargeted proteomic High-efficiency Undecanal-based N-Termini EnRichment (HUNTER) we identified and individually confirmed specific SBT12a target proteins that are involved in plant defense responses and symbiosome maintenance. This positions SBT12a as a central host factor controlling symbiosome performance.

Introduction

The ability of legume plants to form symbiotic associations with nitrogen-fixing rhizobia (root nodule symbiosis; RNS) allows them to overcome nitrogen deficiency in the soil. While this ability has been lost several times independently during evolution, legumes which maintained this unique mutualism, stabilized their intracellular symbionts in newly formed root organs, called nodules, and further compartmentalized them in specialized cell organelles, known as the symbiosomes. Given their tremendous importance and despite their complex nature, nodule-hosted nitrogen-fixing symbiosomes are considered key targets for engineering RNS in non-legume crops to sustainably reduce the amounts of chemical nitrogen fertilizers in agriculture (Huisman & Geurts, 2020, Jhu & Oldroyd, 2023).

Over the past decades, our understanding of the initial molecular dialogue between soil-borne rhizobia and their host plants has advanced considerably (Ghantasala & Roy Choudhury, 2026, Ruan et al., 2026). The corresponding receptors are able, when being stably associated, to trigger nodule organogenesis in the absence of the symbiont (Rübsam et al., 2023). However, these and other spontaneous nodules have so far never been colonized by rhizobia. In legumes, successful infection of the host root and nodules in is achieved by the formation of infection threads (ITs) (de Carvalho-Niebel et al., 2024, Gao et al., 2024). To support polar growth of ITs which enables transcellular progression of rhizobia across several cell layers, host cells

bioRxiv preprint doi: https://doi.org/10.64898/2026.04.09.717438; this version posted April 12, 2026. The copyright holder for this preprint (which was not certified by peer review) is the author/funder, who has granted bioRxiv a license to display the preprint in perpetuity. It is made available under a CC-BY 4.0 International license.

undergo extensive cellular reprogramming that involves local cell wall modifications, membrane repolarization, cytoskeleton rearrangement and cell cycle regulation (Liang et al., 2018, Gao et al., 2022, Lace et al., 2023, Su et al., 2023, Zhang & Ott, 2024, Batzenschlager et al., 2025, Zhao et al., 2025, Qiao et al., 2026). The ultimate step to stabilize the functional symbiosis is the release of the bacteria from nodular ITs (nITs) into infection-competent nodule cells. This step occurs at so-called infection droplets (IDs), bulged and cell wall-free sites of nITs from where thousands of bacteria are pinched off into a single host cell while remain being encapsulated by a plant-derived membrane forming the nitrogen-fixing symbiosome (Adema & Kohlen, 2024, Zhang et al., 2024). At their peak of symbiotic performance, these infected cells are densely packed with bacteria which, in the case of *Medicago truncatula* (hereafter, Medicago) belonging to the inverted repeat-lacking clade (IRLC), terminally differentiate into bacteroids. This state is hallmarked by genome duplications, membrane permeabilization as well as cell elongation, and substantially controlled by a large plant gene family (over 700 members) encoding NODULE-SPECIFIC CYSTEINE-RICH (NCR) peptides (Alunni & Gourion, 2016, Guerra-Garcia & Sankari, 2025). Although exhibiting antimicrobial activity *in vitro*, these NCR peptides, which are targeted to symbiosomes via the DEFECTIVE IN NITROGEN FIXATION (DNF)1-mediated nodule-specific protein secretory pathway, were shown to be crucial for bacteroid survival and differentiation *in planta* (Kim et al., 2015, Wang et al., 2010, Van de Velde et al., 2010). For instance, *NCR169* was identified as a single causal gene in the *dnf7* mutant, which displays impaired bacteroid persistence, premature nodule senescence and reduced nitrogen fixation ability (Horváth et al., 2015), while *NCR343* controls bacteroid maintenance (Zhang et al., 2023, Horváth et al., 2023, Gao et al., 2023). Moreover, accumulating evidence suggests that, in addition to NCR peptides, several other plant factors, such as the phosphatidylinositol-specific phospholipase C-like (PI-PLC) X domain protein DNF2 (Bourcy et al., 2013), the SYMBIOTIC CYSTEINE-RICH RECEPTOR-LIKE KINASE (SymCRK) (Berrabah et al., 2014), NODULES WITH ACTIVATED DEFENSE 1 (NAD1) (Wang et al., 2016), REGULATOR OF SYMBIOSOME DIFFERENTIATION (RSD) (Sinharoy et al., 2013), and NODULE-SPECIFIC POLYCYSTIN-1, LIPOEXYGENASE, α-TOXIN (PLAT) DOMIAN (NPD)

bioRxiv preprint doi: https://doi.org/10.64898/2026.04.09.717438; this version posted April 12, 2026. The copyright holder for this preprint (which was not certified by peer review) is the author/funder, who has granted bioRxiv a license to display the preprint in perpetuity. It is made available under a CC-BY 4.0 International license.

proteins (Pislariu et al., 2019, Trujillo et al., 2019) are also indispensable for bacteroid differentiation. Loss-of-function mutations in any of these genes result in severe defects in symbiosome development, disrupted nodule zonation, and the failure to maintain functional nitrogen-fixing nodules. The tight association between the endoplasmic reticulum (ER), symbiosomes and the plasma membrane also poses challenges to fine-tune targeted secretion and distribution of proteins to the symbiosome membrane/space and the plasma membrane/apoplast. This was recently exemplified for the peribacteroid space. Although being cell wall-free, it requires constant clearing of antimicrobial pectin fragments by lytic enzymes that are continuously secreted into the peribacteroid space (Gao et al., 2025).

These processes further raise the demand for proteases that remove antimicrobial proteins or generate symbiosis-promoting peptides in the peribacteroid space. One of the largest families of proteolytic enzymes responsible are subtilisin-like serine proteases (subtilases, SBTs), which are characterized by a specific arrangement of Asp, His and Ser residues in the catalytic triad. Plant SBTs are typically synthesized as preproenzymes comprising an N-terminal signal peptide for secretion, an inhibitory prodomain that is self-cleaved during maturation, the catalytic domain and the C-terminal fibronectin (Fn) III-like domain (Meyer et al., 2016, Nakagawa et al., 2010). In recent years, subtilases have emerged as critical regulators in plant-microbe interactions (Schaller et al., 2018). For example, during immune responses, plants utilize SBT5.2 to regulate the abundance of elicitors in the apoplast, owing to its ability to cleave the 22-residue flagellin epitope (flg22) at multiple sites (Buscaill et al., 2024). Intriguingly, large-scale phylogenetic analysis of plant subtilases, combined with transcriptomic data, has additionally suggested potential roles for subtilases belonging to the SBT1.13 and SBT1.10 linages in symbiotic interactions (Taylor & Qiu, 2017). Consistent with this, as a representative member from those linages, the *Casuarina glauca* subtilase gene *Cg12* was specifically induced in response to *Frankia* infections (Fournier et al., 2018, Svistoonoff et al., 2003, Laplaze et al., 2000), while its function remains unsolved. The same applies to the subtilases *SbtM1*,*3*,*4* and *SbtS* that are highly activated during arbuscular mycorrhiza symbiosis (AMS) (Kistner et al., 2005, Takeda et al., 2009, Takeda et al., 2011). However, genetic evidence

bioRxiv preprint doi: https://doi.org/10.64898/2026.04.09.717438; this version posted April 12, 2026. The copyright holder for this preprint (which was not certified by peer review) is the author/funder, who has granted bioRxiv a license to display the preprint in perpetuity. It is made available under a CC-BY 4.0 International license.

for the importance of these symbiotic subtilases or of their target proteins have, to our knowledge, never been reported so far. Here, we study a Medicago subtilase, SBT12a, that is specifically induced during RNS and we demonstrate that SBT12a is genetically required for symbiosome maintenance and nitrogen fixation.

Results

SBT12 subtilases are symbiotically regulated in legumes

Although the compartmentalization of efficient nitrogen-fixation in symbiosomes is at the heart of RNS, the mechanisms driving symbiosome stabilization and maturation are sparsely understood. To identify core genetic components, we searched available legume transcriptome data for genes with peaking expressions during nodule formation including their nitrogen-fixing state. These data were cross-referenced with evolutionary datasets, pre-assuming that the core gene set should have been retained in nodulating species. Among them, two proteases, Medtr7g079300 and Medtr7g079310 sparked our interest as their expression strongly correlated with leghemoglobin genes and was associated with symbiotic tissues (Supplementary Fig. 1). Phylogenetically, both genes clustered with members of the subtilase SBT1.13 subfamily (Fig. 1A), the linage that was potentially implicated in symbiotic associations (Taylor & Qiu, 2017). According to the previous nomenclature within this clade (Taylor & Qiu, 2017), we named these subtilases SBT12a (Medtr7g079300, MtrunA17Chr7g0248861) and SBT12b (Medtr7g079310, MtrunA17Chr7g0248871). Interestingly, they are the only members of this clade being significantly upregulated during root nodule symbiosis (Fig. 1A). To gain more confidence on their putative importance for RNS, we reconstructed a phylogenetic tree of SBT12a, SBT12b and their homologs using 100 eudicot species, including 62 species from the nitrogen-fixing clade (NFC) and 38 plant species outside the NFC as outgroups, and combined the phylogeny with available transcriptome data (Libourel et al., 2023) (Supplementary Fig. 2; Table S1). AMS-related expression data was additionally included in the analysis to reflect the symbiotic specificity. First, we determined that *SBT12a* and its paralog *SBT12b*, originate from a recent duplication in the common ancestor of Medicago and *Trifolium pratense* and belong to a single clade, here

bioRxiv preprint doi: https://doi.org/10.64898/2026.04.09.717438; this version posted April 12, 2026. The copyright holder for this preprint (which was not certified by peer review) is the author/funder, who has granted bioRxiv a license to display the preprint in perpetuity. It is made available under a CC-BY 4.0 International license.

named Papilionoid A (Supplementary Fig. 2A). Intriguingly, this clade contains members including SBT12a and SBT12b that specifically respond to RNS. We additionally revealed an additional closely related clade, Papilionoid B, which comprises SBT12 homologs potentially involved in RNS or AMS. Interestingly, the model legume *Lotus japonicus* forming determinate nodules, harbors two SBT12 homologs with one located in a third clade Papilionoid C, suggesting a possible functional divergence between different nodule types during evolution (Supplementary Fig. 2A). Secondly, with few exceptions that mainly exist in the mimosoid clade of legumes, we found that within NFC orders a loss of *SBT12*-related genes frequently occurred in non-nodulating species (Supplementary Fig. 2B). This observation was substantially pronounced in Cucurbitales, where none of the six non-nodulating species harbor copies of *SBT12* homologs while the two nodulators retain it. Furthermore, the transcriptional induction of *SBT12* homologs in *Datisca glomerata* during RNS implies that this gene might have essential symbiotic functions across nodulating species (Libourel et al., 2023). These data support that *SBT12* homologs are well conserved within the NFC, including a possible functional specialization for some of the members.

At the protein level, both SBT12a and SBT12b exhibit a classical plant subtilase topology comprised of an N-terminal signal peptide, an autoinhibitory prodomain, a catalytic domain hosting the catalytic triad (for SBT12a: D154, H226, S551) intersected by a protease associated (PA) domain and a C-terminal region that shares similarities to a fibronectin III domain (Fig. 1B). To further characterize these genes and their possible roles in nodule function, we first recapitulated their transcriptional induction by quantitative Real-Time PCR (qRT-PCR) using a cDNA time course for root infection and nodule development (0-14 dpi). We confirmed significantly increasing transcript levels over time for both *SBT12a* and *SBT12b* (Supplementary Fig. 3, A and C), matching data from published transcriptome datasets (Fig. 1A; Supplementary Fig. 1). To assess spatiotemporal expression dynamics over nodulation process, we cloned their putative promoter regions by selecting 2000 bp upstream of the translational start sites of both *SBT12a* and *SBT12b*, to generate beta-glucuronidase (GUS) reporters. These constructs were transformed into Medicago A17 wild-type (WT) roots, which were subsequently inoculated with *S. meliloti* expressing a beta-galactosidase (lacZ) reporter.

bioRxiv preprint doi: https://doi.org/10.64898/2026.04.09.717438; this version posted April 12, 2026. The copyright holder for this preprint (which was not certified by peer review) is the author/funder, who has granted bioRxiv a license to display the preprint in perpetuity. It is made available under a CC-BY 4.0 International license.

Assessing GUS activity at different symbiotic stages, we detected an activation of the *SBT12a* promoter in infected roots hairs, along the IT trajectory of the root cortex, in nodule primordia and predominantly in the infection/interzone (zone II) of mature nodules (Fig. 1C). By contrast, *SBT12b* promoter activation was closely linked to meristematic tissues, as we detected staining in lateral root primordia and root tips of uninoculated roots, nodule primordia, young nodules and in the apical, meristematic region of mature nodules (Fig. 1D; Supplementary Fig. 3E). These expression patterns are consistent with their spatial transcript abundance retrieved from available single-cell RNA sequencing dataset (Pereira et al., 2024), where *SBT12a* expression was mainly found in putative infected nodule cells that eventually contain nitrogen-fixing symbiosomes, while *SBT12b* transcripts were enriched in tissues with meristematic activity (Supplementary Fig. 3, B and D). Thus, both genes are symbiotically induced and expressed during nodulation, but with the clear distinction that *SBT12a* expression is restricted to infection sites while *SBT12b* is more widely associated with dividing cells. Notably, the rhizobial infection-specific expression pattern of *SBT12a* resemble its *C. glauca* and *Discaria trinervis* homologs, *Cg12* and *Dt12*, of which expression domains were found to be linked to *Frankia* colonization sites during actinorhizal symbiosis (Svistoonoff et al., 2003, Fournier et al., 2018).

sbt12a mutants are severely altered in nitrogen fixation

To investigate their role in RNS genetically, we identified independent exonic mutant alleles for both genes within the *Tnt1* retrotransposon mutant collection (Tadege et al., 2008). Homozygous individuals were isolated for *sbt12a-1* (NF1441), *sbt12a-2* (NF18072), *sbt12b-1* (NF4378) and *sbt12b-2* (NF19394) (Fig. 1B). When grown under fully fertilized (high N) conditions, none of the mutant alleles showed any developmental defects upon scoring shoot and root fresh weight and comparing this to WT R108 plants (Supplementary Fig. 4). By contrast, both *sbt12a* mutant alleles developed severe signs of nitrogen starvation (anthocyanin accumulation, chlorotic leaves) when grown in the absence of an inorganic nitrogen source but in the presence of symbiotic *S. meliloti 2011* (Fig. 1E). In line with this, the shoot fresh weight was significantly reduced in the *sbt12a* mutants (Fig. 1F). To verify that nitrogen fixation capacity

bioRxiv preprint doi: https://doi.org/10.64898/2026.04.09.717438; this version posted April 12, 2026. The copyright holder for this preprint (which was not certified by peer review) is the author/funder, who has granted bioRxiv a license to display the preprint in perpetuity. It is made available under a CC-BY 4.0 International license.

is altered in *sbt12a* mutants, we assayed rhizobial nitrogenase activity within these mutant nodules and found that this was almost fully abolished (Fig. 1G). Accordingly, nodules of both *sbt12a* mutants appeared to be white or greenish (senescent) and less elongated when being scored as early as 21 dpi with *S. meliloti 2011*, while nodules on WT plants were mostly pink (Fig. 1H to H''). To gain cellular resolution of the patterns observed in *stb12a* mutants, we embedded and sectioned young (21 dpi) WT and *sbt12a* nodules and stained them with toluidine blue to visualize bacterial structures. As expected, WT nodules exhibited a dominant fixation zone with densely packed infected cells and a central vacuole scored as "normal" (Fig. 1I to I''). While only few of such infected cells were present in *sbt12a* mutants, these nodules were characterized by a markedly enlarged senescence zone (zone IV) (Fig. 1, I to I''). To further confirm this, we inoculated WT, *sbt12a-1* and *sbt12a-2* mutants with *S. meliloti* carrying a nifH:GUS reporter that is only active in fixing rhizobia and grew these plants for an extended period of 28 days to allow full nodule elongation. While WT nodules with their extended fixation zone were largely stained (Fig. 1J), nodules of *sbt12a-1* and *sbt12a-2* exhibited staining restricted to the apical region and displayed an enlarged, non-stained senescence zone (Fig. 1J' to J''). As a final experiment we genetically rescued this mutant phenotype by introducing a SBT12a-eGFP fusion protein driven by the endogenous *SBT12a* promoter into both *sbt12a* mutant alleles gaining full expansion of the fixation zone in these nodules (Fig. 1K). In contrast, neither the empty vector control (EV) nor the mutant variants being affected in putative propeptide cleavage (D122A) or catalytic activity (S551A) were able to restore the loss-of-function phenotype of the *sbt12a-2* mutant (Fig. 1K). None of these phenotypes was observed on *sbt12b* mutant plants (Supplementary Fig. 5). From these data we concluded that only SBT12a but not SBT12b actively controls nitrogen fixation and therefore only considered SBT12a for the following experiments.

SBT12a controls bacteroid differentiation in symbiosomes

To assess symbiont release as well as bacteroid and symbiosome states in more detail, we first inspected the nodule infection zone (zone II). High magnification toluidine cross-sections revealed the presence of nITs in the WT

bioRxiv preprint doi: https://doi.org/10.64898/2026.04.09.717438; this version posted April 12, 2026. The copyright holder for this preprint (which was not certified by peer review) is the author/funder, who has granted bioRxiv a license to display the preprint in perpetuity. It is made available under a CC-BY 4.0 International license.

(Fig. 2, A and B), which appeared bulky in the *sbt12a-2* mutant (Fig. 2, C and D). In addition to the enlarged senescence zone (Fig. 1, I to II''), *sbt12a* nodules showed clear sign of defects in bacterial release (Fig. 2E). Further ultrastructural analyses of 14 days old nodules by transmission electron microscopy (TEM) revealed the presence of clearly confined nITs in WT nodules (Fig. 2F). In accordance with the light microscopy data (Fig. 2D), nITs were greatly enlarged with occasional intercellular (apoplastic) bacterial release observed in *sbt12a* nodules (Fig. 2G). Upon intracellular release, bacteroids were found to be predominantly rod-shaped in WT nodules (Fig. 2, H and H'). They were, however, smaller and often distorted with a highly enlarged peribacteroid space in *sbt12a-2* mutants (Fig. 2, I and I').

To quantify these differences in bacteroid morphology robustly, we isolated bacteroids from WT and *sbt12a* mutant nodules by fractionation (Fig. 2, J and K). Indeed, bacteroids from WT nodules were significantly longer than those from *sbt12a-2* nodules (Fig. 2, J to L). This indicates that *sbt12a*-derived bacteroids may not reach the differentiation degree and ploidy level as observed in WT nodules. As this can be monitored by the DNA content of these cells, we conducted flow cytometry analysis (FCA) on DAPI-stained bacteroids, considering DAPI intensities of around 10^4 RU as being derived from terminally differentiated bacteroids (Gao et al., 2023). The FCA profiles of bacteroids isolated from young WT nodules showed two dominant peaks, indicating a mixture of young differentiating and older, terminally differentiated bacteroids (Fig. 2M). By contrast, the single FCA peak around 10^3 RU suggested that bacteroids in the *sbt12a* mutant failed to undergo terminal differentiation (Fig. 2N).

Although some bacterial release does occur in *sbt12a* nodules, most of these symbiosomes never reached a fully functional stage. To gain a global insight into how *SBT12a* contributes to symbiosome functionality, we performed bulk RNA sequencing on WT and *sbt12a-2* nodules. We first analyzed the reads mapping to *SBT12a* transcripts in *sbt12a-2* mutant allele. Indeed, a clear deletion within the *SBT12a* transcripts was observed immediately downstream of *Tnt1* retrotransposon insertion site, rendering these transcripts dysfunctional (Supplementary Fig. 6A). Subsequent comparison of the transcriptome profiles revealed the transcriptional induction of 1161 genes in *sbt12a-2*, while 1142

bioRxiv preprint doi: https://doi.org/10.64898/2026.04.09.717438; this version posted April 12, 2026. The copyright holder for this preprint (which was not certified by peer review) is the author/funder, who has granted bioRxiv a license to display the preprint in perpetuity. It is made available under a CC-BY 4.0 International license.

genes were downregulated (Supplementary Fig. 6B; Table S4). When assigning functional categories to these genes, we found a strong repression of classical symbiotic markers in the mutant while several senescence markers including *CYSTEINE PROTEASE* (*CP*) *2*, *CP6* (Berrabah et al., 2023) and *VACUOLAR PROCESSING ENZYME* (*VPE*) (Pierre et al., 2014) were upregulated in *sbt12a* nodules (Fig. 2, O and P; Table S4). This is in line with the fact that *sbt12a* mutant nodules displayed obvious early senescence phenotype. Furthermore, immunity-related genes such as *CHITINASES*, *PATHOGENESIS-RELATED PROTEIN* (*PR*) *10* and *FLAGELLIN SENSING 2* (*FLS2*) were also significantly induced in *sbt12a* nodules (Fig. 2, O and P), indicating that the suppression of defense response was compromised in *sbt12a-2* nodules. In addition, up to 184 prominent regulatory peptides of the NCR family were strongly downregulated in the *sbt12a* mutant (Fig. 2O; Table S4). These includes *NCR169*, *NCR247* and *NCR-new35* (Fig. 2P), for which single loss-of-function mutations have been shown to cause severe defects in symbiosome development and nitrogen fixation (Farkas et al., 2014, Horváth et al., 2015, Horváth et al., 2023). Taken together, these data demonstrate that bacterial differentiation in Medicago nodule cells requires SBT12a.

SBT12a is predominantly secreted to bacterial release sites and into the peribacteroid space

To gain insights into the molecular function of SBT12a, we explored the subcellular localization of the SBT12a protein. For this, we introduced eGFP-tagged SBT12a under the control of its endogenous promoter to Medicago hairy roots. This construct was shown to successfully complement the *sbt12a* mutant phenotype (Fig. 1K). Confocal microscopy analysis revealed that the fluorescent signal was robustly detected in infected cells within transformed nodules. Here, the SBT12a-eGFP fusion protein was initially found to specifically accumulate as small foci around IDs within the infection zone (Fig. 3, A to A"'). Moreover, the signal of SBT12a-eGFP was later predominantly observed in symbiosomes but was excluded from bacteroids, indicating a peribacteroid space localization pattern of SBT12a (Fig. 3, B and C). To rule out that this signal derives from auto-fluorescent molecules within this space, we conducted Fluorescence Lifetime Imaging Microscopy (FLIM) and confirmed

bioRxiv preprint doi: https://doi.org/10.64898/2026.04.09.717438; this version posted April 12, 2026. The copyright holder for this preprint (which was not certified by peer review) is the author/funder, who has granted bioRxiv a license to display the preprint in perpetuity. It is made available under a CC-BY 4.0 International license.

lifetimes of 2.58 ns and 1.51 ns for eGFP and mCherry, respectively (Fig. 3D). These lifetimes resembled values reported earlier for these genetically encoded fluorophores (Lace et al., 2023). These results suggest SBT12a to be a secreted protein in nodule cells, consistent with the presence of a typical signal peptide at N terminus of the protein (Fig. 1B). To further validate symbiosome association, we biochemically fractioned proteins from transformed nodules expressing SBT12a-eGFP, and performed western blot analysis. This confirmed the localization of SBT12a-eGFP in symbiosomes (Fig. 3, E and F), and additionally supports that our isolation protocol is suited to enrich intact symbiosomes from root nodules.

SBT12a is a canonical subtilase identified as a phytaspase

To biochemically characterize SBT12a and shed light on its potential substrates, we ectopically expressed the WT, catalytically inactive (S551A) and putative propeptide cleavage-resistant (D122A) SBT12a variants, each fused to a triple hemagglutinin (HA) tag, in *N. benthamiana* leaf epidermal cells. Apoplastic fluids (AFs) were additionally isolated to determine the secretion of SBT12a. As expected, two bands were detected for WT SBT12a in total extracts, with the predominant one representing the processed form, which was also present in the apoplast fraction (Supplementary Fig. 7A). In contrast, SBT12a variants carrying the D122A, and especially S55A1 mutations remained in the unprocessed zymogen form. As a consequence, none of these mutant forms was efficiently secreted into the apoplast or capable of fully complementing the nodulation phenotype of *sbt12a* mutants (Fig. 1K; Supplementary Fig. 7C). This observation suggests that SBT12a is autocatalytically processed *in planta* and that its serine activity is required for the zymogen maturation and secretion.

To gain information on possible SBT12a target proteins, we first aimed to determine the cleavage specificity of SBT12a. For this purpose, SBT12a was transiently expressed as a HA-fusion protein in *N. benthamiana* leaves and enriched by immunoprecipitation (IP) using HA-traps. The SBT12a (S551A) variant was included as a negative control. To assess whether our recombinant SBT12a has serine hydrolase activity as predicted, we incubated both protein fractions with a Tetramethylrhodamine fluorophosphonate (FP-TAMRA) probe, which specifically and covalently labels serines within enzymatically active

bioRxiv preprint doi: https://doi.org/10.64898/2026.04.09.717438; this version posted April 12, 2026. The copyright holder for this preprint (which was not certified by peer review) is the author/funder, who has granted bioRxiv a license to display the preprint in perpetuity. It is made available under a CC-BY 4.0 International license.

serine hydrolases. Indeed, we observed a clear and strong fluorescent signal at around 90 kDa for the WT SBT12a but not for the catalytic SBT12a (S551A) mutant (Fig. 4A). This demonstrates that SBT12a is indeed an active serine hydrolase. Subsequently, substrate specificity of SBT12a was analyzed by Proteomic Identification of protease Cleavage Sites (PICS) assay (Schilling & Overall, 2008). For this, we incubated our IP-enriched SBT12a protein with an *Escherichia coli* proteome-derived tryptic peptide library and analysed the corresponding cleavage products by mass spectrometry. This identified 205 cleaved peptides that accumulated after incubation with SBT12a (Fig. 4B; Table S5), unambiguously revealing Asp as a dominant residue immediately preceding the cleavage site (P1), and a clear preference for hydrophobic amino acids both upstream (P2 and P3) and downstream (P1' and P2') of the scissile bond (Fig. 4, B and C). This cleavage pattern is highly similar to what has been reported for tomato phytaspase 2 (*Sl*Phyt2), a subtype of subtilase that exhibits strict Asp cleavage selectivity (Reichardt et al., 2020). Our results thus strongly indicated that SBT12a is a *bona fide* phytaspase. In addition, phytaspase identity of SBT12a could also be inferred based on the presence of a diagnostic Asp residue at the prodomain junction site (Fig. 1B). Owing to the autocatalytic cleavage of the prodomain, the sequence at this site is thought to reflect the protease substrate specificity (Reichardt et al., 2018).

Identification of SBT12a substrates using N-terminomics

Having characterized SBT12a as a phytaspase (Fig. 4C) and demonstrated its localization to the peribacteroid space (Fig. 3, B to F), we next aimed to identify its *in vivo* targets within this cellular compartment. To this end, we applied High-efficiency Undecanal-based N-Termini Enrichment (HUNTER), a method for identification of protein N-termini that allows unbiased protease substrate identification (Weng et al., 2019). We isolated intact symbiosomes from WT and the *sbt12a-2* mutant and extracted the corresponding proteins. Primary amines including free amino-termini of *in vivo* cleaved fragments were modified by reductive dimethylation prior to tryptic digestion. The new amino-termini generated by trypsin were subsequently modified with the hydrophobic aldehyde undecanal, enabling their retention on C18 reverse phase cartridges, leaving only the original protein N-termini in the flow-through (Fig. 4D).

bioRxiv preprint doi: https://doi.org/10.64898/2026.04.09.717438; this version posted April 12, 2026. The copyright holder for this preprint (which was not certified by peer review) is the author/funder, who has granted bioRxiv a license to display the preprint in perpetuity. It is made available under a CC-BY 4.0 International license.

Accordingly, high affinity substrates of SBT12a are expected to accumulate in their processed (cleaved) form in WT, while remaining in their unprocessed (uncleaved) form in the *sbt12a* mutant samples.

Mass spectrometric analysis identified 19541 N-terminal peptides, with 1740 originating from Medicago, and 17801 from rhizobia. To identify candidate SBT12a cleavage products, we first limited the dataset to reliably quantified peptides (quantified in ≥ 50% of replicates or exclusively detected in ≥ 3 replicates of one condition) mapping to positions within the protein model (position < 8, to exclude freshly synthesized or aminopeptidase-processed proteins). The resulting dataset contained 509 neo-N-terminal peptides from Medicago, with 31 exclusively found in WT but not in *sbt12a-2* mutant nodules and 37 N-terminal peptides significantly enriched ($q \leq 0.05$) in WT (Fig. 4E; Table S6). In addition, 24 neo-N-terminal peptides of rhizobial origin were solely detected in the WT and 235 significantly accumulated in WT with respect to the mutant. Further alignment of all these 327 protease-generated N-terminal peptides showed a pronounced selectivity for Asp at the P1 position, along with a preference for hydrophobic residues both upstream and downstream of the putative cleavage sites (Fig. 4F). This pattern largely resembles the substrate specificity of SBT12a determined by the in vitro PICS assay (Fig. 4C). Of these candidate substrates harboring an Asp at P1, the abundance of the two Medicago NCR peptides, NCR039 and NCR361, was found to be markedly accumulated in the WT compared to the *sbt12a* mutant (Fig. 4E; Table S6). This implies that SBT12a might be involved in the processing of NCRs in nodules. Although, plant mutants of these NCRs have not been reported by now, the phenotypes of other NCR mutants such as *dnf7* (NCR169), *dnf4* (NCR211), *NF-FN9363* (NCR343), *sym19/20* (NCR-new35) resemble the one of the *sbt12a* mutant (Horváth et al., 2023). Interestingly, in recent years phytaspases have been implicated in the maturation of peptide hormones. For instance, tomato *Sl*Phyt1 and *Sl*Phyt2 could cleave prosystemin to regulate defense signaling, while *Sl*Phyt2 additionally process phytosulfokine precursors in response to drought stress, thereby promoting flower abscission (Beloshistov et al., 2018, Reichardt et al., 2020). Here, a similar activation mechanism may apply to SBT12a and these candidate NCR peptides.

bioRxiv preprint doi: https://doi.org/10.64898/2026.04.09.717438; this version posted April 12, 2026. The copyright holder for this preprint (which was not certified by peer review) is the author/funder, who has granted bioRxiv a license to display the preprint in perpetuity. It is made available under a CC-BY 4.0 International license.

Notably, peptides mapping to the Medicago DNF2 protein were found to be exclusively present in the WT (Fig. 4E; Table S6). Previous studies have reported an essential role of DNF2 in maintaining bacteroid viability during nitrogen fixation (Bourcy et al., 2013). As the *dnf2* mutant phenocopies *sbt12a* we assume that both proteins act synergistically to regulate symbiosome development. Moreover, multiple peptides derived from NPD family proteins, including NPD5 and NPD1, accumulates exclusively (NPD5) and significantly (NPD1) in the WT than in the mutant (Fig. 4E; Table S6). Likewise, the *npd1* mutant and multigene *NPD* knockout lines, to a large extent, phenocopy the *sbt12a* mutant, indicating an additional functional link between these proteins (Pislariu et al., 2019, Trujillo et al., 2019).

To further verify these putative host substrate proteins, we performed cleavage assays using quenched peptides (QP) as also applied for other proteases (Buscaill et al., 2024, Chen et al., 2024). In the intact peptide, close proximity between the quencher and the fluorophore in the non-cleaved peptide prevents fluorescence emission, an effect that is abolished upon peptide cleavage (Fig. 4G). For this, we designed and custom-synthesized QPs containing cleavage sites from DNF2, NPD5 and NPD1, and exposed them to purified, recombinant active SBT12a as well as the catalytically inactive SBT12a (S551A) variant. Indeed, we observed high levels of fluorescence emission for DNF2 and NPD5 and lower levels for NPD1, confirming that these proteins are indeed direct targets of SBT12a (Fig. 4H-J). Taken together, our data prove that loss-of function mutations in *SBT12a* lead to altered proteolytic processing of host proteins, including DNF2, NPDs, NCRs, and also rhizobia proteins. Thus, we conclude that SBT12a controls symbiosome integrity by mediating proteolysis of those and additional substrates.

Discussion

During legume-rhizobial interactions, symbiosome formation and differentiation represent the key steps in the transition from initial infection and organogenesis to nitrogen fixation within nodules (Zhang et al., 2024). To accommodate thousands of those newly formed organelles in a single cell, the host undergoes extensive cellular adaptations involving the reorientation of endocytic/exocytic

bioRxiv preprint doi: https://doi.org/10.64898/2026.04.09.717438; this version posted April 12, 2026. The copyright holder for this preprint (which was not certified by peer review) is the author/funder, who has granted bioRxiv a license to display the preprint in perpetuity. It is made available under a CC-BY 4.0 International license.

pathways (Harrison & Ivanov, 2017), structural reconfigurations of common organelles, in particular vacuoles and the ER (Zhang et al., 2022, Yang et al., 2023), and fine-tuning of various signaling responses (Ren et al., 2025). Intriguingly, recent studies have underpinned the importance of symbiosomes for the evolutionary stabilization of nitrogen fixation in legumes (de Faria et al., 2022, Casaes et al., 2024). However, our knowledge about how host cells tightly monitor and maintain symbiosome integrity over time to achieve sufficient nitrogen fixation is limited. Here, we uncovered a specific protease in Medicago, SBT12a, to be central in this process. In nodules, SBT12a is specifically secreted to symbiotic compartments, IDs and the peribacteroid space where its continuous proteolytic activity in the peribacteroid space secures sustained symbiosome differentiation and nitrogen fixation. This involves SBT12a-mediated processing substrates of plant and/or rhizobial origin (Supplementary Fig. 8).

Comparable to other canonical plant subtilases (Schaller et al., 2018), SBT12a follows the secretory pathway in a prodomain-dependent manner (Supplementary Fig. 7A), which in nodules may involve the action of the DNF1-containg signal peptidase complex (Wang et al., 2010). This is supported by the fact that both *SBT12a* and *DNF1* shared largely overlapped expression domains in the infection zone of mature nodules (Fig. 1C) (Wang et al., 2010). Accumulation of SBT12a around IDs suggests a role in bacterial release (Fig 3, A to A"'). Indeed, corresponding defects were clearly observed in *sbt12a* nodules (Fig. 2, C to G). Given the similarities with other subtilases, it is tempting to hypothesize that SBT12a might be involved in the processing of cell wall modifying enzymes around IDs facilitating bacterial release (Sénéchal et al., 2014, Su et al., 2023, Zhao et al., 2025). Apart from IDs, SBT12a predominantly localizes to the peribacteroid space within the nodular fixation zone (Fig. 4, B to F). This localization is spatially distinct from its expression domain in the nodular infection zone (Fig. 1C), indicating sustained stability of the SBT12a protein in the fixation zone. Considering that such spatial separation has also been shown for other symbiosome (membrane) localized proteins such as SYMREM1 and NCR (Lefebvre et al., 2010, Horváth et al., 2023). we assume that protein loading of symbiosomes mainly occurs during bacterial release from IDs and early bacteroid differentiation.

bioRxiv preprint doi: https://doi.org/10.64898/2026.04.09.717438; this version posted April 12, 2026. The copyright holder for this preprint (which was not certified by peer review) is the author/funder, who has granted bioRxiv a license to display the preprint in perpetuity. It is made available under a CC-BY 4.0 International license.

The possibility to isolate these symbiotic organelles allowed us to apply quantitative proteomics and the identification of putative SBT12a substrates (Demir et al., 2018). Our HUNTER analysis revealed 68 and 259 N-terminal peptides derived from Medicago and rhizobia, respectively, that were more abundant in WT than in the mutant (Fig. 4E; Table S6). Given that neo-N-termini represent a direct signature of protease activity, which should only occur in the WT but not in the mutant, we focused on those candidates for further analysis. Surprisingly, systematic profiling of potential “cleavage windows” from all these 327 peptides uncovered a cleavage specificity pattern similar to that observed in the PICS assay, with a dominant presence of Asp at P1 position (Fig. 4, C and F). This not only confirms the strict Asp-dependent cleavage specificity of SBT12a but also validates the robustness of our proteomic approaches.

Among plant-derived candidate substrates, Medicago DNF2, NPD5 and NPD1 caught our main attention as they were reported to be involved in symbiotic nitrogen fixation (Bourcy et al., 2013, Pislariu et al., 2019, Trujillo et al., 2019). Bacterial differentiation and viability were strongly impaired in loss-of-function *dnf2* nodules, and typical defense markers including *PR* genes were activated (Bourcy et al., 2013), which is similar to what we observed in *sbt12a* nodules (Fig. 2, H to P; Table S4). However, as an atypical PI-PLC protein lacking part of the catalytic core, the mechanism by which DNF2 participates in dampening defense response during bacteroid differentiation remains unclear (Bourcy et al., 2013). Our data indicates that this process likely involves SBT12a-mediated proteolysis. This is supported by data from QP assays showing that SBT12a was indeed capable of directly and efficiently cleaving the DNF2 peptide (Fig. 4H). We therefore propose that SBT12a modifies DNF2, thereby modulating host immune responses to create a permissive environment for bacteroid persistence. Similar scenarios may also apply to NPD family proteins, as we observed clear processing of NPD1- and NPD5-derived peptides by SBT12a, albeit with different efficiencies (Fig. 4, I and J).

In recent years, the involvement of plant subtilases, and also phytaspases, in peptide signaling through selective processing of peptide precursors to release mature peptides has been shown (Deng et al., 2025). In nodules of IRLC legumes including Medicago, terminal differentiation of bacteria is specifically controlled by mature NCR peptides (usually 35-55 residues in length) that are

bioRxiv preprint doi: https://doi.org/10.64898/2026.04.09.717438; this version posted April 12, 2026. The copyright holder for this preprint (which was not certified by peer review) is the author/funder, who has granted bioRxiv a license to display the preprint in perpetuity. It is made available under a CC-BY 4.0 International license.

delivered from host cells to symbiosomes (Alunni & Gourion, 2016, Guerra-Garcia & Sankari, 2025). While several NCRs are processed by DNF1 during secretion (Wang et al., 2010), further modifications of these peptides are unknown. Identifying NCR039 and NCR361 in our proteomic profiles suggest that SBT12a may serve such functions. Exploiting over 200 rhizobia-derived N-terminal peptides during HUNTER analysis, it is very likely that several SBT12a substrates are of rhizobial origin (Fig. 4E; Table S6). Supporting this possibility, cross-species proteolytic processing by subtilases has recently been demonstrated for *N. benthamiana* SBT5.2. In that system, SBT5.2 fine-tunes immune responses by directly inactivating the immunogenicity of bacteria-derived molecules, such as flagellin and CSPs, in the apoplast (Buscaill et al., 2024, Chen et al., 2024). On the other hand, the possibility that SBT12a may be responsible for a non-selective protein turnover (including potential antimicrobial components) cannot be excluded. Other subtilases, such as melon cucumisin and Arabidopsis SBT1.7, have been indicated to play such roles (Schaller et al., 2018). This indicates that continuous removal of specific proteins would be required for symbiosome stabilization as recently proposed for cell wall-related proteins (Gao et al., 2025).

In summary, our study determined SBT12a as a core factor in Medicago, functioning as a symbiosis-specific subtilase/phytaspase that controls nitrogen fixation in root nodules by modulating proteolytic processes within the peribacteroid space. Future studies, particularly those employing biochemical and genetic approaches, will be required to fully understand how SBT12a-mediated substrate processing contributes to symbiosome performance.

Methods

Plant materials and growth conditions

Two *Medicago truncatula* (Medicago) ecotypes, Jemalong A17 and R108 were used in this study. All *Tnt1* insertion lines including *sbt12a-1* (NF1441), *sbt12a-2* (NF18072), *sbt12b-1* (NF4378) and *sbt12b-2* (NF19394) generated in the R108 background were obtained from Medicago Mutant Database (Oklahoma State University, USA).

bioRxiv preprint doi: https://doi.org/10.64898/2026.04.09.717438; this version posted April 12, 2026. The copyright holder for this preprint (which was not certified by peer review) is the author/funder, who has granted bioRxiv a license to display the preprint in perpetuity. It is made available under a CC-BY 4.0 International license.

Medicago seeds were scarified in 96% sulfuric acid (H_2SO_4) for ten minutes followed by rinsing six times with sterile tap water. The washing steps were repeated again after treatment with a bleach solution containing 1.2% sodium hypochlorite (NaClO) and 0.1% sodium dodecyl sulfate (SDS) for 1 minute. Seeds were germinated on 1% water agar plates in the dark at 22°C for 20 hours after vernalization at 4°C for 5 days. Germinated seedings were either transferred to pots filled with 1:1 (v/v) mixtures of quartz sand and vermiculite and kept in a growth chamber with 16 hours light/8 hours dark photoperiod at 24°C for one week before rhizobial inoculation (for phenotyping), or subjected to hairy root transformation.

Wild type *Nicotiana benthamiana* plants were grown in a growth chamber (22°C, 16 hours light/8 hours dark).

Hairy root transformation and rhizobial inoculation

Hairy root transformation of Medicago plants was performed as described previously (Boisson-Dernier et al., 2001). In brief, seed coats were removed from germinated seedlings and a cut was made 5 mm below the cotyledons using a sterile blade. The wound area was then dipped into solid culture of *Agrobacterium rhizogenes* ARqua1 carrying the corresponding binary vector. Transformed seedlings were placed on Fahräeus medium supplemented with 0.5 mM NH_4NO_3 and kept vertically at 21°C in the dark for 3 days, followed by 4 days under a 16 h light/8 h dark photoperiod in a growth chamber, with the root part shaded in the darkness. Next, seedlings were transferred into fresh Fahräeus medium and grown for another ten days under the same growth conditions. Positive roots were selected based on nuclear fluorescent selection maker using a stereo microscope. The transformed plants were then transferred to a mixture of quartz sand and vermiculite (1:1) in pots and inoculated with rhizobia after one week.

Sinorhizobium meliloti strain 2011 (Sm2011), Sm2011 *hemA::lacZ*, Sm2011 *nifH::GUS* or Sm2011 mCherry were used for the inoculation of Medicago roots. For this, the Sm2011 strain was first cultured on solid TY medium supplemented with appropriate antibiotics for 3 days at 28°C. Freshly grown Sm2011 cells were then used to inoculate liquid TY medium and cultured for 24 hours at 28°C with shaking. Rhizobial cells were harvested by centrifugation at 3000 rpm for

bioRxiv preprint doi: https://doi.org/10.64898/2026.04.09.717438; this version posted April 12, 2026. The copyright holder for this preprint (which was not certified by peer review) is the author/funder, who has granted bioRxiv a license to display the preprint in perpetuity. It is made available under a CC-BY 4.0 International license.

10 minutes, and the resulting pellet was resuspended in liquid Fahräeus medium to a final concentration of OD_{600} = 0.005. Each plant was inoculated with 10 mL of rhizobial suspension. Plants were watered with sterile tap water (30 mL/pot) and fertilized with liquid Fahräeus medium (30 mL/pot) once a week.

Phylogenetic analysis

To identify putative SBT genes in Medicago, the S8 domain of known SBT proteins was used as query sequences to perform BLAST searches against Medicago genome (https://phytozome-next.jgi.doe.gov/info/Mtruncatula_Mt4_0v1). The obtained SBT sequences were further manually examined by the criteria of the presence of I9 prodomain and all four conserved residues (Asp, His, Asn and Ser) essential for catalytic function in the S8 domain. All SBT sequences were aligned using the ClustalW program with default parameters and a phylogenetic tree was constructed using the neighbor-joining method in MEGA11 software.

To reconstruct the phylogeny of plant subtilases, we first made a database of proteomes from 100 eudicot species, including 29 species from Fabales, 15 species from Rosales, 9 species from Fagales, and 9 species from Cucurbitales (Table S1). The sequences of SBT12a (Medtr7g079300) and SBT12b (Medtr7g079310) were aligned against this database using blastp 2.16.0+ (Camacho et al., 2009), with the following parameters: “-outfmt 6 -evalue 10e-5-word_size -max_target_seqs 999999”. The 7570 sequences from this blast search were aligned using MAFFT v7.526 (Katoh & Standley, 2013) with default parameters and trimmed with trimAL v1.4.rev15 (Capella-Gutiérrez et al., 2009) with the parameter -gt 0.05. A preliminary phylogeny was reconstructed using fasttree v2.1.11 using default parameters (Price et al., 2010). This dataset was reduced in multiple steps by keeping only the closest related sequences to SBT12a and SBT12b, to eventually have a dataset consisting of subtilases that originated form a single copy in the common ancestor of land plants. This set of 262 sequences were aligned with MAFFT using the L-INS-I method, followed by trimming with trimAL with the parameter -gt 0.2. Model testing was performed using IQ-tree v2.2.2.3 with the parameter -m TESTNEWONLY (Minh

bioRxiv preprint doi: https://doi.org/10.64898/2026.04.09.717438; this version posted April 12, 2026. The copyright holder for this preprint (which was not certified by peer review) is the author/funder, who has granted bioRxiv a license to display the preprint in perpetuity. It is made available under a CC-BY 4.0 International license.

et al., 2020, Kalyaanamoorthy et al., 2017). The best model based on the Bayesian Information Criterion (BIC) was Q.plant+I+R8 (Minh et al., 2021). A more complex model test was done based on this model by additionally including the profile mixture models C10-C60 (Quang le et al., 2008). The best model based on BIC was again chosen, and the tree was reconstructed with that model with IQ-TREE using the following parameters: "-m Q.plant+C60+F+I+R8 --ufboot 1000 --alrt 1000 --mix-opt --wbtl" (Guindon et al., 2010, Minh et al., 2013). Expression levels of genes were determined using the summarized data provided by a previous study (Libourel et al., 2023). For nodulation, up- and downregulation was based on the columns ending on "WSR_Nod_Up" and "WSR_Nod_Down". Expression during arbuscular myccorhizal symbiosis was extracted for *M. truncatula* from the column starting with "Medtru_Myct" and for *L. japonicus* from the columns "Lotjap_Myc_Down" and Lotjap_Myc_Up. The phylogeny and related data were visualized in R v4.2.2 (Team, 2022) using the tidyverse metapackage and the packages ggtree v3.15.0, ggtreeExtra v1.8.1, ggnewscale 0.5.1, phytools 2.4-4 and ape 5.8-1 (Yu et al., 2016, Revell, 2024, Paradis & Schliep, 2019).

Molecular cloning

For plasmids expressed in Medicago, the Golden Gate cloning system was used (Weber et al., 2011). The open reading frame of *SBT12a* was amplified from Medicago Jemalong A17 by PCR using a primer pair with the appropriate overhangs designed for subsequent Golden Gate assembly, and cloned into pJET1.2/blunt vector (Thermo Scientific) followed by Sanger sequencing confirmation. The pJET1.2-SBT12a was further used as a template to generate point mutations by PCR in order to eliminate internal BsaI or BpiI restriction sites, or to create active site mutants of *SBT12a* if needed. Putative promoters of both *SBT12a* and *SBT12b* comprising 2 kb upstream of the start codon were retrieved from the Phytozome database (https://phytozome-next.jgi.doe.gov/), and synthesized by Life Technologies after in silico removal of internal BsaI or BpiI restriction sites present in the sequences. All other functional Level 0 modules used for Golden Gate assembly in this study were obtained from the ENSA project collection (https://www.ensa.ac.uk/). For expression of *SBT12a*

bioRxiv preprint doi: https://doi.org/10.64898/2026.04.09.717438; this version posted April 12, 2026. The copyright holder for this preprint (which was not certified by peer review) is the author/funder, who has granted bioRxiv a license to display the preprint in perpetuity. It is made available under a CC-BY 4.0 International license.

and its mutant variants in *N. benthamiana*, the expression vector pPPO70v1HA was used (Li et al., 2022). *SBT12a* and its mutant variants fused to triple hemagglutinin (HA) tag were amplified using the primers containing *SmaI* and *XbaI* restriction sites. The fragments were then ligated into pPPO70v1HA cut with *SmaI* and *XbaI*. All primers used in this study are listed in the Table S2. Details of all constructs are listed in the Table S3.

RNA extraction and quantitative Real-Time PCR

Total RNA was isolated from root or nodule samples harvested at indicated time points using the Spectrum Plant Total RNA Kit (Sigma Life Science) according to the manufacturer's instructions. Subsequently, 1 µg of total RNA was used for cDNA synthesis using SuperScript III Reverse Transcriptase (Invitrogen). The resulting cDNA was diluted 1:5 and 1 µL was used for quantitative Real-Time PCR (qRT-PCR) analysis, which was performed using SYBR Green Master Mix (Applied Biosystems) and a StepOnePlus Real-Time PCR System. Gene expression levels were normalized to a ubiquitin gene used as the internal reference (Liang et al., 2021). Primers used for the analysis are listed in Table S2.

Acetylene reduction assay

Acetylene reduction assay was conducted as described previously (Yun et al., 2023). In brief, nodulated roots of each plant were collected in a 50 mL vial with a flanged rubber septum. Air was replaced with an equal volume of acetylene using a syringe. Samples were then incubated for 2 hours at 28°C before quantification of ethylene by gas chromatography (GC-4100; EQAI, China). The nitrogenase activity was calculated as the amount of ethylene produced per plant per hour.

Nodule sections

For semi-thin sections, nodules collected at indicated time points were firstly fixed in buffer Z (0.1 M phosphate buffer (pH 7.0), 10 mM KCl, 1 mM $MgCl_2$) containing 2% glutaraldehyde at room temperature for 1 hour. After 3 times washing in buffer Z, fixed nodule tissues were dehydrated in a graded

bioRxiv preprint doi: https://doi.org/10.64898/2026.04.09.717438; this version posted April 12, 2026. The copyright holder for this preprint (which was not certified by peer review) is the author/funder, who has granted bioRxiv a license to display the preprint in perpetuity. It is made available under a CC-BY 4.0 International license.

ethanol/water series (50%, 70%, 80%, 90% and 100%) for 1 hour each at room temperature and then subjected to Technovit 7100 (Heraeus Kulzer) resin embedding system according to the supplier's instructions. Longitudinal sections (10 µm thickness) were made using a RM2245 microtome (Leica Biosystems, Germany).

To assess the protein localization of SBT12a, transformed nodules generated via hairy root transformation were freshly collected and embedded in 6.5 % low melting agarose (Biozym Scientific, Hessisch Oldendorf, Germany). Nodule sections (70 µm thickness) were obtained using a VT1000S vibratome (Leica Biosystems, Germany).

Histochemical staining

GUS staining was performed as reported previously with minor modifications (Lee et al., 2024). Briefly, roots or nodules harvested at various time points were washed thoroughly and fixed in 2% (v/v) glutaraldehyde at room temperature for 1 hour. After rinsing three times in washing solution containing 50 mM phosphate buffer (pH 7.2), the fixed tissues were immersed in GUS reaction buffer, vacuum-infiltrated for 20 minutes, and incubated at 37°C for 2–4 hours. The GUS reaction was terminated by washing the samples in the same buffer. Stained samples were stored in 70% ethanol until imaging or further subjected to X-Gal staining.

For X-Gal staining, nodulated tissues were immersed in buffer Z supplemented with 0.8 mg mL^{-1} X-Gal and 5 mM each of $K_3Fe(CN)_6$ and $K_4Fe(CN)_6$. Samples were vacuum-infiltrated for 20 minutes and subsequently incubated at 28°C overnight until sufficient staining was achieved.

Toluidine blue staining of nodule sections was performed as previously described (Xiao et al., 2014).

Sample preparation for transmission electron microscopy

WT and *sbt12a-2* mutant nodules harvested at indicated timepoints were cut in half and immediately submerged in 4% paraformaldehyde (PFA) and 2.5% glutaraldehyde in MTSB buffer. Vacuum was applied for 15 minutes and samples were left in the fixative for 3 hours at room temperature, transferred to

bioRxiv preprint doi: https://doi.org/10.64898/2026.04.09.717438; this version posted April 12, 2026. The copyright holder for this preprint (which was not certified by peer review) is the author/funder, who has granted bioRxiv a license to display the preprint in perpetuity. It is made available under a CC-BY 4.0 International license.

4°C and kept overnight. After primary fixation, samples were washed five times with MTSB buffer and post-fixed in aqueous 1% O_SO_4 for 2 hours at room temperature, washed and *in bloc* stained for 2 hours in 2% UrAc. Dehydration was carried out in a graded ethanol/water series (50%, 70%, 80% and 95%-15 minutes each), followed by 30 minutes in 100% ethanol and 100% acetone. Samples were then embedded in Epoxy resin. Ultrathin sections (70 nm) were obtained using a Reichert-Jung Ultracut-E microtome and examined using a Hitachi 7800 TEM coupled to a Xarosa CMOS camera (Emsis).

Confocal microscopy and Fluorescence Lifetime Imaging Microscopy (FLIM)

Fluorescence imaging was conducted using a TCS SP8 confocal microscope (Leica Microsystems, Mannheim, Germany). Images were acquired with a 20×/0.75 and a 40×/1.10 (HC PL APO CS2) water immersion lens. A White Light Laser (WLL) was used as an excitation source. eGFP was excited at 488 nm, and the emission was collected at 500–550 nm. mCherry was excited at 561 nm, and the emission was detected in the 600–650 nm range. FLIM analysis was performed as previously described (Lace et al., 2023). All images were processed and analyzed using Fiji/ImageJ software.

Nodule fractionation and symbiosome isolation

Nodule fractionation and symbiosome isolation was carried out following the procedure described previously (Catalano et al., 2004). In brief, WT and mutant nodules were cut off from roots and homogenized in a prechilled extraction solution (0.5 M sucrose, 50 mM Tris/HCl (pH 7.4), 10 mM DTT and 1 x Protease Inhibitor Cocktail (Rochel)). The homogenate was filtered through two layers of Miracloth and labelled as nodule total proteins. This resulting suspension was further spun at 10000 g for 1 minute at 4°C, and the supernatant and pellet were labelled as cytosol and symbiosome proteins, respectively. The pellet was resuspended in extraction buffer and washed two more times sequentially in 1.5 M and 1 M sucrose buffer each containing 50 mM Tris/HCl (pH 7.4), 10 mM DTT and 1 x Protease Inhibitor Cocktail. The final symbiosome pellet was resuspended in extraction solution for further analysis.

bioRxiv preprint doi: https://doi.org/10.64898/2026.04.09.717438; this version posted April 12, 2026. The copyright holder for this preprint (which was not certified by peer review) is the author/funder, who has granted bioRxiv a license to display the preprint in perpetuity. It is made available under a CC-BY 4.0 International license.

Flow cytometry assay

To investigate the role of SBT12a in bacteroid differentiation, bacteroids were isolated from WT and *sbt12a-2* mutant nodules as previously described (Horváth et al., 2023), and subsequently stained with 5 µg/mL DAPI. Flow cytometry analysis was performed using a BD LSRFortessa™ flow cytometer (BD Biosciences). A total of 50,000 bacteroids were analyzed, and the resulting data were processed using FlowJo software.

RNA sequencing analysis

Three biological replicates using WT and *sbt12a-2* mutant nodules harvested at 18 dpi were prepared for RNA sequencing. Total RNA was extracted as described above, and its quality and concentration were assessed using an Agilent 2100 Bioanalyzer. Library preparation and sequencing were carried out by Novogene Co., Ltd. (Beijing, China). Sequencing data were analyzed using the Galaxy bioinformatics platform (https://usegalaxy.eu/) following standard procedures. Briefly, raw reads were quality-checked and mapped to the Medicago reference genome (https://medicago.toulouse.inra.fr/MtrunA17r5.0-ANR/) using the STAR aligner. Gene-level read counts were generated using STAR, and differentially expressed genes (DEGs) were identified with the DESeq2 package, applying a threshold of $\log_2$ fold change > 1 and adjusted *P*-value < 0.05.

Transient expression in N. benthamiana and protein extraction

Agrobacterium tumefaciens strain GV3101 was used for agroinfiltration of 4 to 5-week-old *N. benthamiana* leaves. Freshly cultivated agrobacteria harboring expression constructs and p19 silencing suppressor were harvested by centrifugation (4000 g, 10 minutes) and resuspended in an infiltration buffer (10 mM $MgCl_2$, 10 mM MES (pH 5.6), 150 µM acetosyringone). The cultures were diluted and mixed to obtain a final OD_{600} of 0.7 each. After 2 hours of incubation, bacterial cells were infiltrated into *N. benthamiana* leaves using needle-less syringes. The infiltrated plants were kept in a growth chamber until use.

bioRxiv preprint doi: https://doi.org/10.64898/2026.04.09.717438; this version posted April 12, 2026. The copyright holder for this preprint (which was not certified by peer review) is the author/funder, who has granted bioRxiv a license to display the preprint in perpetuity. It is made available under a CC-BY 4.0 International license.

For total protein extraction, leaves harvested 4 days after infiltration were ground in liquid nitrogen and suspended in extraction buffer containing 50 mM Tris/HCl (pH 7.5), 100 mM NaCl, 0.5% Triton X-100, 10 mM β-mercaptoethanol and 1 x Protease Inhibitor Cocktail (Roche). Extracts were then centrifuged at 16000 g for 10 minutes at 4°C. The resulting supernatant was used for measurement of protein concentrations by the dye-binding Bradford assay (Bio-Rad). Protein extracts were flash-frozen in liquid nitrogen and stored at -80°C until further analyses.

.

Isolation of apoplastic fluids

Apoplastic fluids (AFs) were collected as previously reported (Reichardt et al., 2018). Briefly, agroinfiltrated *N. benthamiana* leaves were submerged in ice-cold extraction buffer (50 mM NaH_2PO_4/Na_2HPO_4 (pH 6.5), 200 mM KCl) and vacuum infiltrated for 5 minutes. Excess water on the surface of leaves was dried off with absorbing paper, and leaves were mounted into a 25 mL syringe placed in a 50 mL tube. AFs were collected by centrifugation at 1500 g at 4 °C for 7 minutes, and stored at -20°C for further use.

Western blot

For immunodetection, protein samples were separated by 12% SDS-polyacrylamide gel electrophoresis (PAGE), and transferred to a polyvinylidene difluoride (PVDF) membrane (0.2 µm pore size) using the Trans-Blot® Turbo™ semi-dry transfer system (Bio-Rad). After being blocked with 5% (w/v) powder milk diluted in TBS-T for 1 hour at room temperature, the membrane was hybridized with a primary antibody anti-GFP (Takara Bio Cat# 632381; 1:5000) or peroxidase-conjugated anti-HA (Roche, Germany, Cat# 12013819001; 1:4000), at 4 °C overnight. The membrane was washed 3 times in TBS-T for 30 minutes. Peroxidase-conjugated secondary antibodies (anti-mouse, Sigma-Aldrich Cat# A4416; 1:5000) was applied, if required, for 2 hours at room temperature. Signals were visualized using the Clarity Western ECL Substrate (Bio-Rad) on an ECL ChemoCam Imager (Intas Science imaging).

bioRxiv preprint doi: https://doi.org/10.64898/2026.04.09.717438; this version posted April 12, 2026. The copyright holder for this preprint (which was not certified by peer review) is the author/funder, who has granted bioRxiv a license to display the preprint in perpetuity. It is made available under a CC-BY 4.0 International license.

Immunoprecipitation

Total protein was extracted from *N. benthamiana* leaves transiently expressing SBT12a-3xHA or SBT12a (S551A)-3xHA using the same extraction buffer as mentioned above but without adding protease inhibitors. 10 mL of each protein sample was incubated with 40 µL HA-Trap Magnetic Agarose (ChromoTek) at 4 °C for 1 hour with gentle rotation. Beads were then washed five times with washing buffer (10 mM Tris/HCl (pH 7.5), 150 mM NaCl and 0.5 mM EDTA). Bound proteins were subsequently eluted using 500 µM HA peptide (ChromoTek), and the protein concentration was determined using the Bradford assay.

Activity-based protein profiling (ABPP)

FP-TAMRA probe (Thermo Scientific) was used to label and detect active subtilases. The probe was dissolved in 100 µL of DMSO to make a 0.1 mM stock solution. 10 µL of immunoprecipitated SBT12a or SBT12a (S551A) were incubated with 0.2 µM FP-TAMRA in PBS (pH 7.0) for 1 hour at room temperature in the dark. The reaction was stopped by adding 2 x SDS sample buffer and boiling for 5 minutes. Labeled proteins were analyzed by SDS-PAGE followed by fluorescent gel scanning with a Typhoon FLA 9000 (GE Healthcare Life Sciences) using Cy3 settings (532 nm excitation, 610PB filter).

Proteomic Identification of Cleavage Sites

An *Escherichia coli* (strain K12) proteome-derived peptide library was generated by whole cell proteome digestion with trypsin as described (Demir et al., 2022a). Aliquots of 5 µg purified tryptic peptide libraries were equilibrated in PBS (pH 7.0) buffer. IP-enriched recombinant SBT12a or catalytically inactive SBT12a (S551A) were added and incubated for 2 hours at 25°C. Four replicate reactions were performed for each construct. As a modification to the original protocol (Demir et al., 2022b), the resulting peptide samples were not modified by dimethylation but directly stopped by acidification, individually desalted using self-packed three-layer SDB-RPS StageTips, reconstituted in 0.1% TFA and loaded onto Evotips (Evosep) for label-free analysis.

bioRxiv preprint doi: https://doi.org/10.64898/2026.04.09.717438; this version posted April 12, 2026. The copyright holder for this preprint (which was not certified by peer review) is the author/funder, who has granted bioRxiv a license to display the preprint in perpetuity. It is made available under a CC-BY 4.0 International license.

Enrichment of N-terminal peptides

N-terminal peptides were enriched with the HUNTER method as previously described (Stockert et al., 2024). Briefly, proteomes were extracted with a denaturing extraction buffer (6 M guanidine hydrochloride, 100 mM HEPES (pH 7.4)), followed by reduction with 10 mM DTT and cysteine carbamidomethylation with 50 mM CAA. An estimated 100 µg of protein per replicate was purified with paramagnetic SP3 beads (Cytiva). Primary amines were labelled by reductive dimethylation with heavy formaldehyde ($^{12}CD_2O$). The reaction was quenched and samples were digested overnight with trypsin (1:100 w/w) at 37°C. Subsequently, 10 µg of peptides were withdrawn to determine labelling efficiency (pre-HUNTER). Newly generated tryptic peptides bearing primary amines were modified with 100 mM undecanal and removed using reversed-phase HRX spin cartridges (Macherey & Nagel). N-terminal peptides remaining in the flow-through were desalted by self-packed three-layer C18 StageTips (Rappsilber et al., 2007) and reconstituted in 0.1% TFA.

Mass spectrometry data acquisition

Peptide samples were measured on an Exploris 480 mass spectrometer (Thermo Scientific) coupled to nanoflow chromatography systems. For HUNTER samples, peptides were separated with an Ultimate 3000 RSLCnano system (Thermo Scientific), loaded on a µPAC C18 trapping column (Thermo Scientific) with flow rate of 10 µL/minutes and separated on a µPAC C18 pillar array analytical column (50 cm bed length; Thermo Scientific) at a flow of 0.5 µL/minute. Both columns were kept at 40°C. Peptides were eluted using a binary solvent system consisting of 0.1% formic acid (solvent A) and 86% acetonitrile with 0.1% formic acid (solvent B). Mobile phase B increased as follows: 1% to 4% over 2 minutes, 4% to 25% over 24 minutes, 25% to 44% over 12 minutes, and a final column wash at 90% B for 4 minutes. Peptide were introduced into the mass spectrometer with a NanoSpray Flex ion source (Thermo Scientific) equipped with the µPAC Flex iON Connect and a fused silica emitter (20 µm inner diameter, 10 µm tip inner diameter, 360 µm outer diameter; New objective). The source voltage was set to +1.8 kV and the ion transfer tube temperature to 275°C. Peptides of PICS samples were separated with 44 minutes gradient on an Evosep One system (EvoSep) equipped with a

bioRxiv preprint doi: https://doi.org/10.64898/2026.04.09.717438; this version posted April 12, 2026. The copyright holder for this preprint (which was not certified by peer review) is the author/funder, who has granted bioRxiv a license to display the preprint in perpetuity. It is made available under a CC-BY 4.0 International license.

nano-LC column (EV1137, 15 cm × 150 µm, Evosep) maintained at 40°C by a column oven (PRSVO-V2, Sonation). The binary solvent system consisted of 0.1% formic acid (solvent A) and 100% acetonitrile with 0.1% formic acid (solvent B) and operated in the 30 SPD mode. For electrospray ionization, a stainless-steel emitter with an integrated liquid junction (EV1072, Evosep) was mounted into an EasySpray adapter and installed in a NanoSpray Flex ion source (Thermo Scientific). The spray voltage was set to +2.0 kV and the ion transfer tube temperature to 275°C. Data were acquired in data-independent acquisition (DIA) mode. Each acquisition cycle comprised one MS1 survey scan (m/z 350–1400, resolution 120,000, RF lens 40%, AGC target 300%, maximum injection time 45 ms), followed by MS2 fragment ion scans in profile mode (resolution 30,000, RF lens 50%, AGC target 1000%, maximum injection time 54 ms, variable isolation window width with 1 m/z overlap).

Mass spectrometry data analysis

Acquired DIA data were analysed with FragPipe v24.0 (Yu et al., 2023) with the integrated MSFragger (v4.4.1) search engine. For HUNTER data, peptide spectra were predicted from the Medicago and *S. meliloti 2011* proteome databases, with enzyme specificity set to semi-specific cleavage with variable N-terminus and C-terminal ArgC digest, up to two missed cleavages, peptide length of 7–45 amino acids, precursor mass range of 200–5,000 Da, and a maximum of five variable modifications per peptide. Dimethylation at protein N-termini and lysine side chains (+32.0564 Da) and cysteine carbamidomethylation (+57.0215 Da) were set as fixed modifications. Variable modifications included methionine oxidation (+15.9949 Da), acetylation of peptide N-termini and lysines (+9.9541 Da), N-terminal pyroglutamate formation from glutamine (-49.0829 Da) or glutamic acid (-50.0699 Da), and proline monomethylation (-16.0282 Da). For PICS data, spectra were matched against the UniProt canonical *Escherichia coli* (strain K12) proteome (downloaded 2026-03-02, 4,531 entries), with cleavage specificity set to semi-specific cleavage with variable N-terminus and C-terminal trypsin digest, up to two missed cleavages, peptide length of 7–40 amino acids, precursor mass range of 300–5,000 Da, and a maximum of four variable modifications per peptide. Cysteine carbamidomethylation (+57.0215 Da) was set as fixed

bioRxiv preprint doi: https://doi.org/10.64898/2026.04.09.717438; this version posted April 12, 2026. The copyright holder for this preprint (which was not certified by peer review) is the author/funder, who has granted bioRxiv a license to display the preprint in perpetuity. It is made available under a CC-BY 4.0 International license.

modification. Variable modifications included methionine oxidation (+15.9949 Da), and acetylation of peptide N-termini and lysines (+42.01056). Peptide and protein identifications were subjected to stringent quality filtering, with a 1% false discovery rate threshold applied at both the peptide-spectrum match and protein levels using Philosopher (v5.1.3-RC9). Identified peptides where quantified with DIA-NN (v1.8.2 beta 8) (Demichev et al., 2020) as implemented in the FragPipe package.

Peptide tables were filtered to retain only peptides quantified in at least 50% of replicates per condition for the N-termini enrichment experiment, and in at least 75% of replicates for the PICS experiment. Peptides exclusively observed in at least three replicates of one condition were likewise retained in both datasets. N-terminal peptides with a start position of ≤ 7 were excluded. Peptides sharing the same start position and N-terminal modification status but differing solely in methionine oxidation state or charge were collapsed into a single entry by summing their intensities. Differential abundance of N-terminal peptides between WT and *sbt12a-2* mutant samples was analyzed using the LIMMA package in R (Ritchie et al., 2015). Linear modeling with empirical Bayes moderation was applied to compute moderated *t*-statistics, p-values, and q-values, with $\log_2$ fold changes derived from replicate means. Changes in N-terminal peptide abundance supported by a LIMMA-moderated q-value < 0.05 were considered significant.

Quenched peptide assays

The quenched peptides (QPs) derived from candidate substrate proteins were commercially synthesized with a DABCYL modification at the N-terminus and an EDANS modification at the C-terminus (GenScript) at a purity of 95%. The assay was performed as previously reported. The synthesized peptides were resuspended in DMSO to prepare a 1 mM stock solution, which was further diluted in water to 200 µM. Immunoprecipitated SBT12a or SBT12a (S551A) were mixed with QPs to a final concentration of 10 µM in a total volume of 100 µL. Fluorescence was recorded at 25°C for 2 hours using microplate reader (POLARstar Omega, BMG LABTECH, Ortenberg, Germany) with excitation and emission wavelengths set to 335 nm and 493 nm, respectively.

bioRxiv preprint doi: https://doi.org/10.64898/2026.04.09.717438; this version posted April 12, 2026. The copyright holder for this preprint (which was not certified by peer review) is the author/funder, who has granted bioRxiv a license to display the preprint in perpetuity. It is made available under a CC-BY 4.0 International license.

Quantification and statistical analysis

All statistical analyses and generation of graphs were performed using GraphPad Prism software (version 9.5.1; GraphPad Software Inc.). The normality of the data was evaluated to determine the appropriate statistical method to be used. Brown–Forsythe and Welch ANOVA followed by Dunnett's T3 multiple comparisons test was applied as parametric analyses. For non-parametric data, Kruskal–Wallis followed by Dunn's multiple comparisons or Mann–Whitney tests were conducted. Sample size and statistical significance level have been indicated in the respective figure legends.

Data availability

The mass spectrometry proteomics data have been deposited to the ProteomeXchange Consortium (Deutsch et al., 2023) via the PRIDE partner repository (Perez-Riverol et al., 2025) with the dataset identifiers PXD076390 for the HUNTER N-terminome data (Reviewer access token: hDUfTNzPSYEY) and PXD076264 for PICS data (Reviewer access token: xrYmY77Zs3Z2).

Acknowledgements

We would like to thank Rosula Hinnenberg, Eija Schulze and Carmen Schubert for their excellent technical support, and the entire team for constructive discussions on the project and critical reviewing of the manuscript. We also acknowledge the staff of the Life Imaging Center (LIC) at the Hilde Mangold House (HMH), Albert-Ludwigs-University of Freiburg, for their support with confocal microscopy. Furthermore, we are grateful to Prof. Andreas Hiltbrunner for providing pPPO70v1HA plasmid. This work was supported by Enabling Nutrient Symbioses in Agriculture (ENSA) project, which was funded by Gates Agricultural Innovations (G1164932/57461) (P.M.D., T.O.), the German Research Foundation (DFG) under Germany's Excellence strategy (CIBSS-EXC-2189 - project ID 390939984 to S.H., C.K., P.F.H., T.O.; SFB 1381 - project ID 403222702 to C.K., P.F.H., T.O.; SFB 1403- project ID 414786233 to P.F.H.) and the China Scholarship Council (CSC) grant 202006300033 (G.Z.).

bioRxiv preprint doi: https://doi.org/10.64898/2026.04.09.717438; this version posted April 12, 2026. The copyright holder for this preprint (which was not certified by peer review) is the author/funder, who has granted bioRxiv a license to display the preprint in perpetuity. It is made available under a CC-BY 4.0 International license.

Author contributions

Conceptualization, G.Z. and T.O.; Investigation, G.Z., F.S., M.M., M.R.F., F.V.B., C.H.R., B.L., W.Y., N.N., H.M.; Provided unpublished data: M.Y.J.; Provided help in data analysis: A.M., S.H., N.N.; Supervision of individual project parts: C.K., C.S., P.M.D., P.F.H., T.O.; Writing-original draft, G.Z. and T.O.; Writing-review & editing, G.Z., F.S., M.M., M.R.F., F.V.B., W.Y., C.H.R., B.L., H.M., M.Y.J., A.M., S.H., C.K., C.S., P.M.D., P.H., and T.O.; Funding acquisition, G.Z., P.M.D., P.F.H., and T.O.; Supervision, T.O.

Declaration of interests

The authors declare that a patent application has been submitted (WO/2024/009146).

bioRxiv preprint doi: https://doi.org/10.64898/2026.04.09.717438; this version posted April 12, 2026. The copyright holder for this preprint (which was not certified by peer review) is the author/funder, who has granted bioRxiv a license to display the preprint in perpetuity. It is made available under a CC-BY 4.0 International license.

Figures and legends

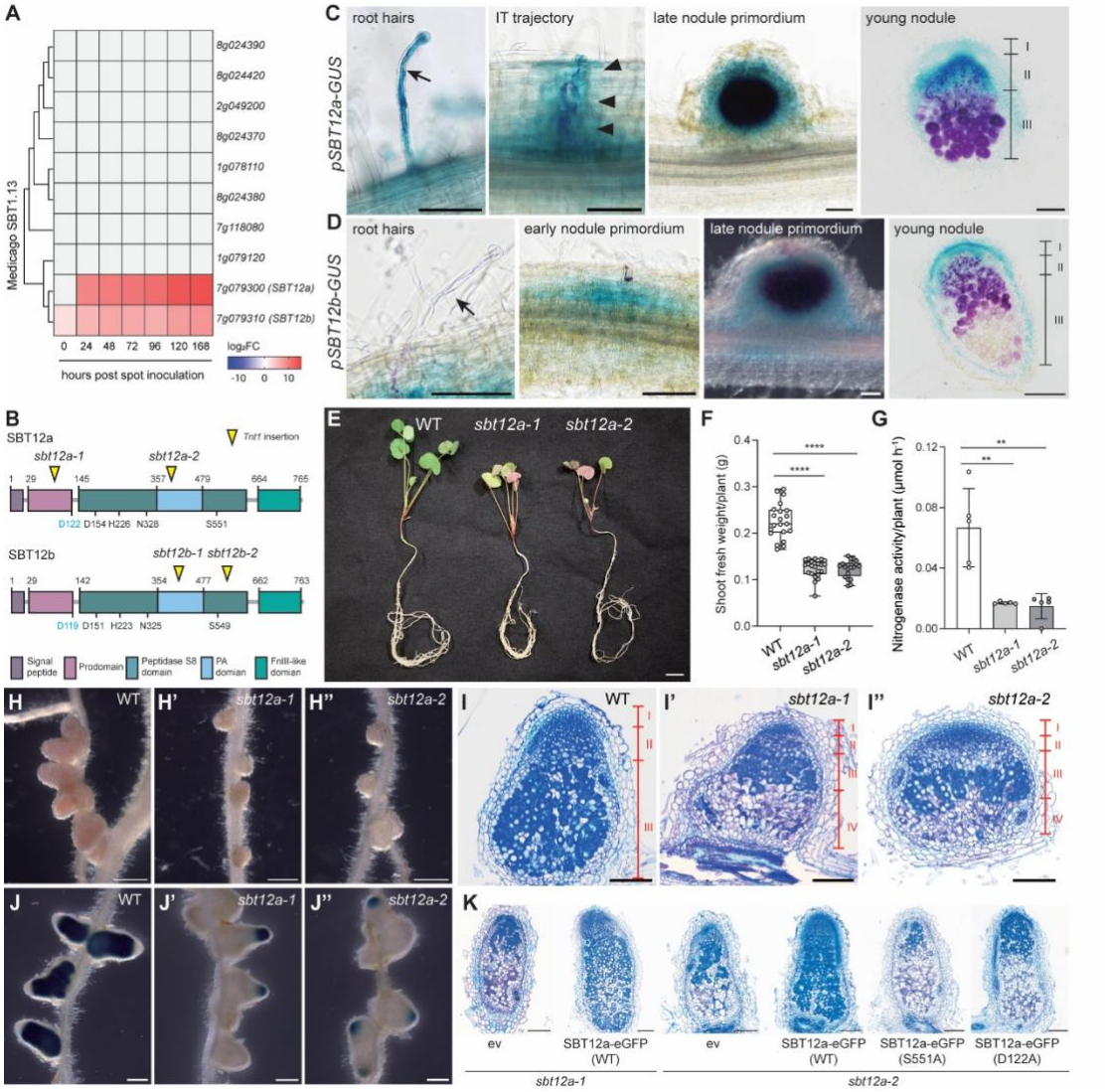
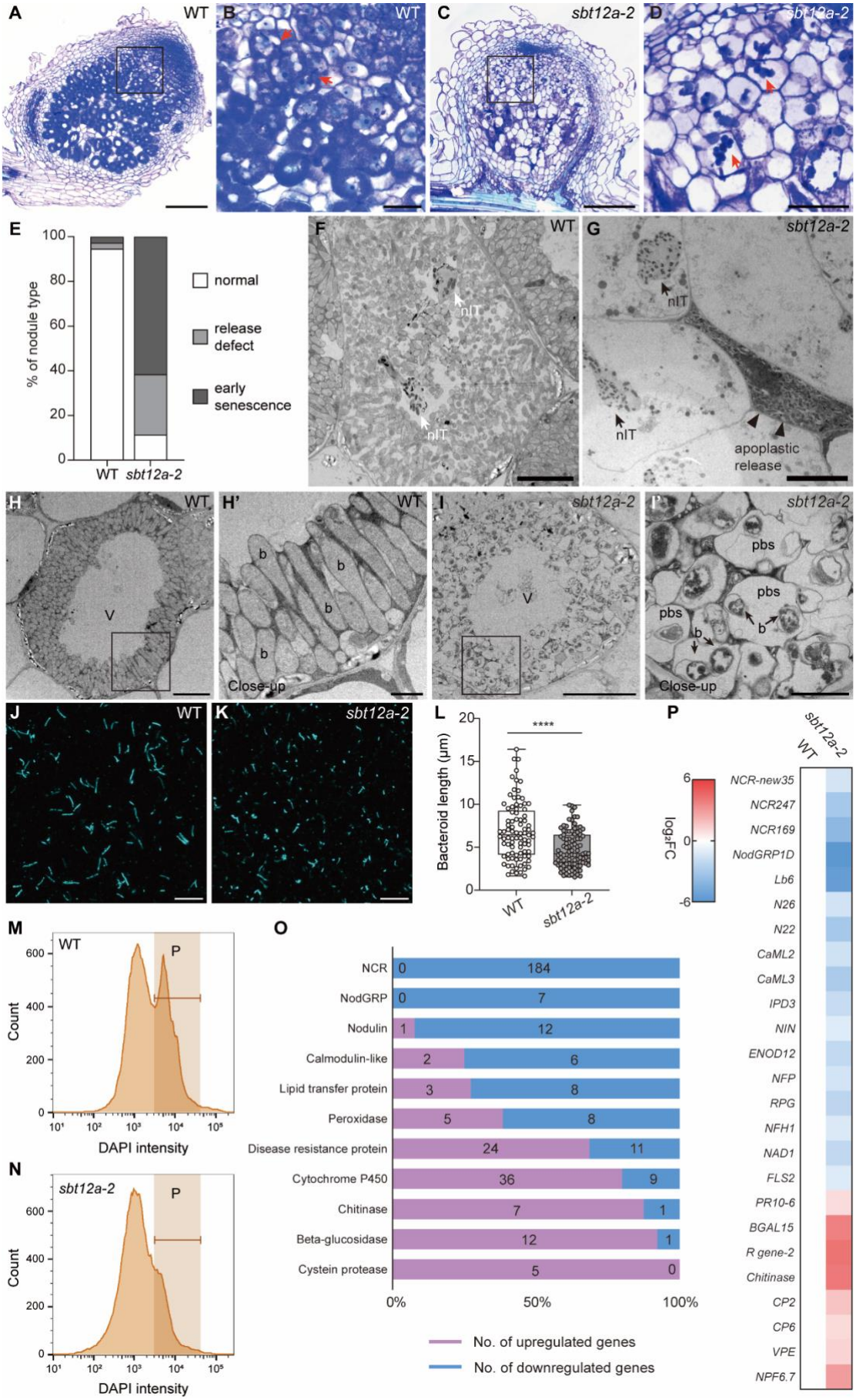


Fig. 1. *SBT12a* is induced during rhizobial symbiosis and affects nitrogen fixation. (**A**) Phylogenetic and expression analysis of Medicago subtilases belonging to the SBT1.13 clade. The phylogenetic tree was generated from the alignment of subtilase sequences retrieved from the Phytozome v13 database (https://phytozome-next.jgi.doe.gov/) using the neighbor-joining method. The symbiosis-related expression data for each gene were obtained from the previous study (Schiessl et al., 2019). (**B**) Schematic primary structure of the SBT12a and SBT12b proteins. Different domains were predicted by InterPro (https://www.ebi.ac.uk/interpro/) and labeled with different colors. Black numbers indicate domain junctions and active amino acid residues. Asp at the prodomain removal site were additionally labelled with blue. Arrowheads indicate positions of the *Tnt1* insertion. (**C** and **D**) Promoter-GUS assays visualizing the expression domains of *SBT12a* (C) and *SBT12b* (D) throughout the nodulation process. GUS activity and *Sinorhizobium meliloti 2011*-expressed *LacZ* were stained blue and magenta, respectively. Arrows indicate infection threads (ITs) in root hair cells and arrowheads indicate ITs penetrating from epidermis to inner cortical layers (IT trajectory). Different zones were marked in longitudinal sections of elongated nodules. zone I, meristem; zone II, infection zone; zone III, fixation zone. Scale bars, 100 μm. (**E** and **F**) *sbt12a* mutant seedlings displayed nitrogen-defective growth phenotype (E) at 21 dpi with *S. meliloti 2011*. Scale bar, 1 cm. Shoot fresh weight was quantified (F). n=21, 22 and 20 for WT, *sbt12a-*

bioRxiv preprint doi: https://doi.org/10.64898/2026.04.09.717438; this version posted April 12, 2026. The copyright holder for this preprint (which was not certified by peer review) is the author/funder, who has granted bioRxiv a license to display the preprint in perpetuity. It is made available under a CC-BY 4.0 International license.

1 and *sbt12a-2*, respectively. Statistically significant differences were analyzed using Mann-Whitney test. **** p<0.0001. (**G**) Acetylene reduction assay (ARA) showing the disrupted nitrogen fixation capacity of *sbt12a* mutant compared to WT plants. n=5 for all genotypes. Each data point represents the mean value of 5 plants. Statistically significant differences were analyzed using Mann-Whitney test. ** p<0.01. The ARA experiment was independently repeated twice with similar results. (**H** to **H''**) Representative nodules formed on WT and *sbt12a* mutant roots at 21 dpi with *S. meliloti 2011*. Scale bars, 1 mm. (**I** to **I''**) Longitudinal sections of nodules from (H) showing premature senescence induced by *sbt12a* mutation, as demonstrated by an expanded zone IV (senescence zone). Sections were counterstained with 0.05% (w/v) toluidine blue. Scale bars, 200 µm. (**J** to **J''**) Representative nodules formed on WT and *sbt12a* mutant roots at 28 dpi with *S. meliloti 2011* carrying a *pnifH::GUS* reporter enabling visualization of zones with active nitrogen fixation. Scale bars, 500 µm. Phenotyping was independently repeated four times with similar results. (**K**) Genetic complementation analysis showing that the premature senescence phenotype of *sbt12a* mutant nodules was restored by introduction of the WT SBT12a, but not by the two mutant variants (S551A and D122A). Transformed nodules were harvested 28 dpi with *S. meliloti 2011* and longitudinally sectioned. Scale bars, 200 µm.

bioRxiv preprint doi: https://doi.org/10.64898/2026.04.09.717438; this version posted April 12, 2026. The copyright holder for this preprint (which was not certified by peer review) is the author/funder, who has granted bioRxiv a license to display the preprint in perpetuity. It is made available under a CC-BY 4.0 International license.



bioRxiv preprint doi: https://doi.org/10.64898/2026.04.09.717438; this version posted April 12, 2026. The copyright holder for this preprint (which was not certified by peer review) is the author/funder, who has granted bioRxiv a license to display the preprint in perpetuity. It is made available under a CC-BY 4.0 International license.

Fig. 2. The *sbt12a* mutant is impaired in bacteroid differentiation.
(**A** and **B**) Longitudinal section of WT nodules collected 14 dpi with *S. meliloti 2011*. Rhizobia were normally released from nodular infection threads (nITs), indicated by arrows, and colonized host cells in WT nodules. (B) is a close-up image of the rectangle marked region in (A). Scale bars, 200 μm (A), 50 μm (B). (**C** and **D**) In the *sbt12a-2* mutant nodules rhizobia were frequently blocked in swelled nITs. (D) is a close-up image of the rectangle marked region in (C). Scale bars, 200 μm (C), 50 μm (D). (**E**) Quantification of WT and *sbt12a-2* nodules showing normal colonization (like in A and B), defective rhizobial release (like in C and D) and early senescence. 38 WT and 56 mutant nodules were randomly collected for sections from two independent replicates. (**F**) Transmission electron microscopy (TEM) analysis revealing typical rhizobial release sites in an infected WT nodule cell. Scale bar, 10 μm. (**G**) Colonization defects exemplified by enlarged nITs in largely uncolonized cells and apoplastic bacterial release (arrowhead) observed in *sbt12a-2* mutant nodules. Scale bar, 10 μm. Data were collected from more than twelve nodules at 14 dpi for each genotype in two independent replicates. (**H** to **I**) TEM analysis of nodule cells in WT (H) and *sbt12a-2* (I). Symbiosome structures in *sbt12a-2* are markedly disorganized with enlarged peribacteroid spaces and multiple small bacteroids enclosed in a single symbiosome. b, bacteroid. pbs, peribacteroid space. V, central vacuole. (H') and (I') are close-up images of the regions marked by rectangle in (H) and (I), respectively. Scale bars, 10 μm (H and I), 2 μm (H' and I'). Data were collected from ten nodules at 21 dpi for each genotype in two independent replicates. (**J** and **K**) Representative confocal images of isolated bacteroids stained with DAPI (cyan) from WT (J) and *sbt12a-2* mutant (K) nodules collected at 21 dpi. Scale bars, 20 μm. (**L**) Quantification of bacteroids length. n=89 and 98 for WT and *sbt12a-2*, respectively. Statistical differences were analyzed using Mann-Whitney test. **** $p<0.0001$. (**M** and **N**) Flow cytometry analysis of DAPI-stained bacteroids isolated from WT (M) and *sbt12a-2* mutant (N) nodules. Up to 50000 bacteroids from each WT and mutant nodules were examined in the analysis. P represents bacteroid populations that exhibit the same DAPI intensity. Experiments for bacteroids phenotyping were repeated three times with similar results. (**O**) Classification of representative differentially expressed genes (DEGs) across gene families. Numbers of up-regulated and down-regulated genes (*sbt12a-2* vs WT) are indicated for each gene family, and are labelled with pink and blue backgrounds, respectively. (**P**) The expression of representative DEGs from transcriptome data.

bioRxiv preprint doi: https://doi.org/10.64898/2026.04.09.717438; this version posted April 12, 2026. The copyright holder for this preprint (which was not certified by peer review) is the author/funder, who has granted bioRxiv a license to display the preprint in perpetuity. It is made available under a CC-BY 4.0 International license.

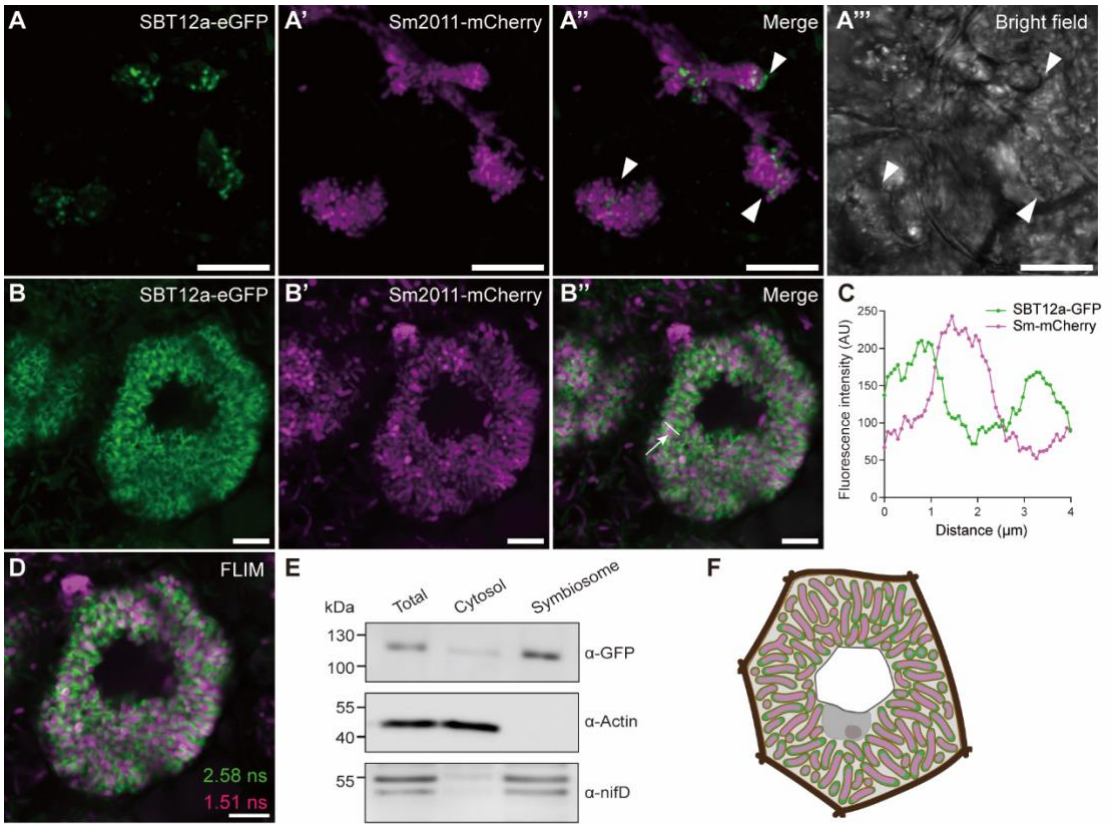


Fig. 3. SBT12a localizes at rhizobial release sites and at the peribacteroid space in infected nodule cells.

(**A** and **B**) Confocal microscopy images showing the localization of SBT12a-eGFP (green) at putative rhizobial release sites (A) and the peribacteroid space (PBS) (B) in infected nodule cells. Nodules infected with mCherry-producing *S. meliloti 2011* (magenta) and expressing SBT12a-eGFP were collected at 28 dpi and 70 µm sections were used for confocal imaging. White arrowheads indicate the site of rhizobial release. Scale bars, 10 µm. (**C**) Fluorescence intensities measured along the linear transect (arrow) from (B''). (**D**) PBS localization pattern of SBT12a-eGFP analyzed by Fluorescence Lifetime Imaging Microscopy (FLIM). The lifetimes for eGFP and mCherry measured by FLIM are indicated. More than 20 nodules from multiple transgenic roots were analyzed in three independent replicates. Scale bar, 10 µm. (**E**) Immunoblot assay showing that SBT12a-eGFP is targeted to the symbiosome. Protein samples were obtained from the following fractions: Total, total nodule extracts; Cytosol, cytosolic fragments of nodule cells; Symbiosome, isolated symbiosomes. α-actin and α-nifD were used as controls for the cytosolic and the symbiosome fraction, respectively. Western blot was repeated twice from two independent rounds of hairy root transformation. (**F**) Schematic illustrations of SBT12a (green) localized to the peribacteroid space surrounding bacteroids (magenta) within symbiosomes.

bioRxiv preprint doi: https://doi.org/10.64898/2026.04.09.717438; this version posted April 12, 2026. The copyright holder for this preprint (which was not certified by peer review) is the author/funder, who has granted bioRxiv a license to display the preprint in perpetuity. It is made available under a CC-BY 4.0 International license.

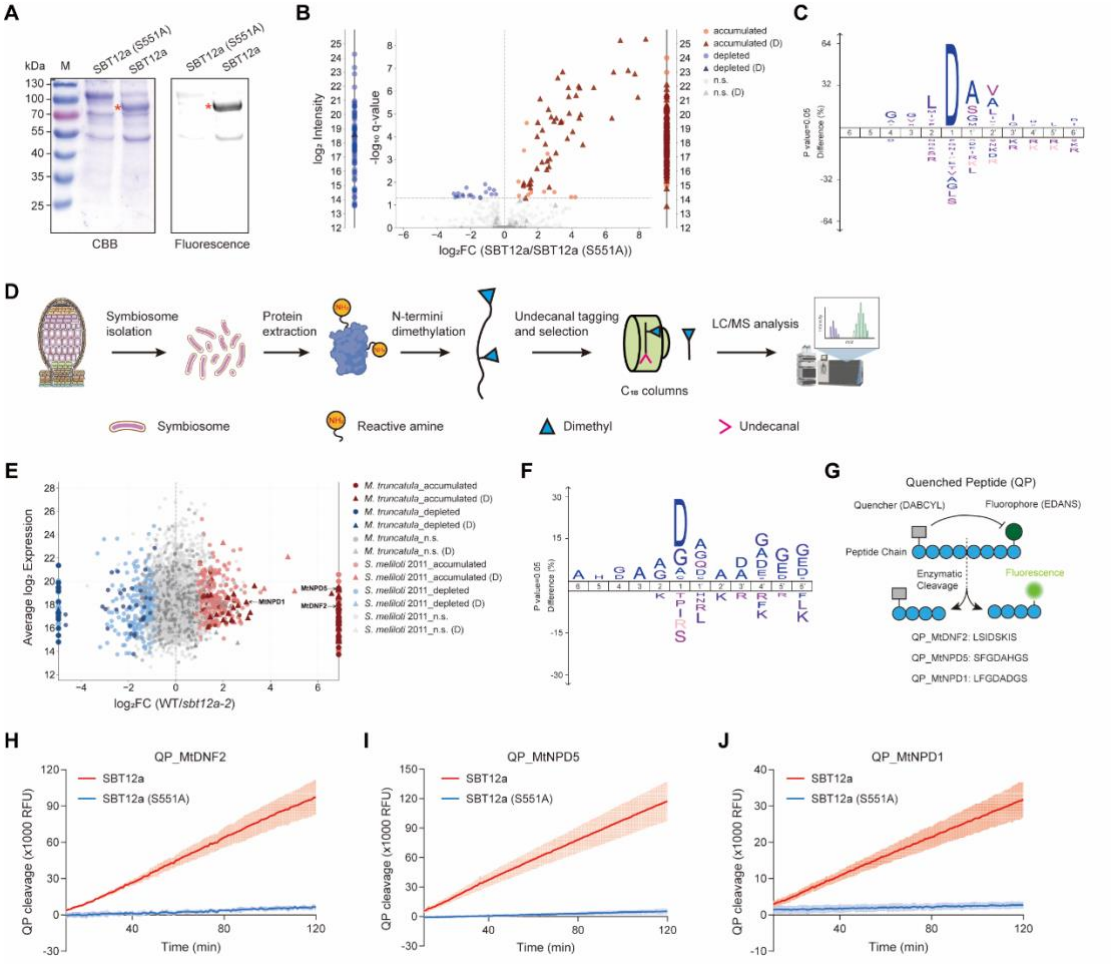


Fig. 4. SBT12a mediates Asp-specific proteolytic regulation in symbiosomes.
(**A**) Immunoprecipitation of SBT12a-3xHA and SBT12a-3xHA (S551A) (used as the negative control. Proteins were labelled with 0.2 µM FP-TAMRA and separated on SDS-PAGE followed by Coomassie Brilliant Blue (CBB) staining, or in-gel fluorescence. Red asterisks indicate the mature form of SBT12a-3xHA after self-processing. (**B** and **C**) Analysis of substrate specificity of SBT12a by Proteomics Identification of Cleavage Sites (PICS) assay. (B) shows the abundance of peptides quantified in at least two of four biological replicates after incubation with SBT12a and SBT12a (S551A). Peptides detected exclusively in at least three out of four replicates of one condition but absent in the other are displayed on $\log_2$-transformed intensity scales on either side of the volcano plot. Light and dark red indicate increased abundance, light and dark blue indicate decreased abundance, and grey indicates no significant change after treatment with SBT12a compared to SBT12a (S551A) as determined by a LIMMA-moderated *t*-test with FDR correction ($q < 0.05$). Triangles mark peptides resulting from cleavage after Asp. (C) is the IceLogos showing over- and underrepresented amino acid residues observed preceding (positions 1-6) and following (positions 1'-6') SBT12a cleavage sites derived from the significantly accumulating peptides. (**D**) Schematic representation of the High-efficiency Undecanal-based N Termini EnRichment (HUNTER) pipeline. Some components were created with BioRender.com. (**E**) Abundance of identified N-terminal peptides in WT compared to *sbt12a-2* mutant, with N-termini identified in only one genotype plotted on one side. Peptides shown in red represent N-terminal peptides that were either significantly enriched ($q < 0.05$) or exclusively found in at least three out of four biological replicates in WT. Blue indicates N-terminal peptides significantly enriched or exclusively observed in *sbt12a-2*. Triangle symbols denote peptides resulting from cleavage with Asp preceding the cleavage site. (**F**) IceLogo representations of the amino acid sequence context surrounding the scissile bond, derived from N-terminal peptides that were exclusively and significantly enriched in the WT background. (**G**) Conceptual illustration of using quenched peptides (QPs) to monitor processing. Three QPs from MtDNF2, MtNPD5 and MtNPD1 containing the putative cleavage sites detected by HUNTER were custom-synthesized. (**H** to **J**) Processing of MtDNF2 (H), MtNPD5 (I) and

bioRxiv preprint doi: https://doi.org/10.64898/2026.04.09.717438; this version posted April 12, 2026. The copyright holder for this preprint (which was not certified by peer review) is the author/funder, who has granted bioRxiv a license to display the preprint in perpetuity. It is made available under a CC-BY 4.0 International license.

MtNPD1 (J)-derived QPs by SBT12a. 0.4 µg of SBT12a-3xHA proteins were used and incubated with 10 µM QPs. The lines represent the mean value of 4 independent replicates and the shading represents the standard deviation.

bioRxiv preprint doi: https://doi.org/10.64898/2026.04.09.717438; this version posted April 12, 2026. The copyright holder for this preprint (which was not certified by peer review) is the author/funder, who has granted bioRxiv a license to display the preprint in perpetuity. It is made available under a CC-BY 4.0 International license.

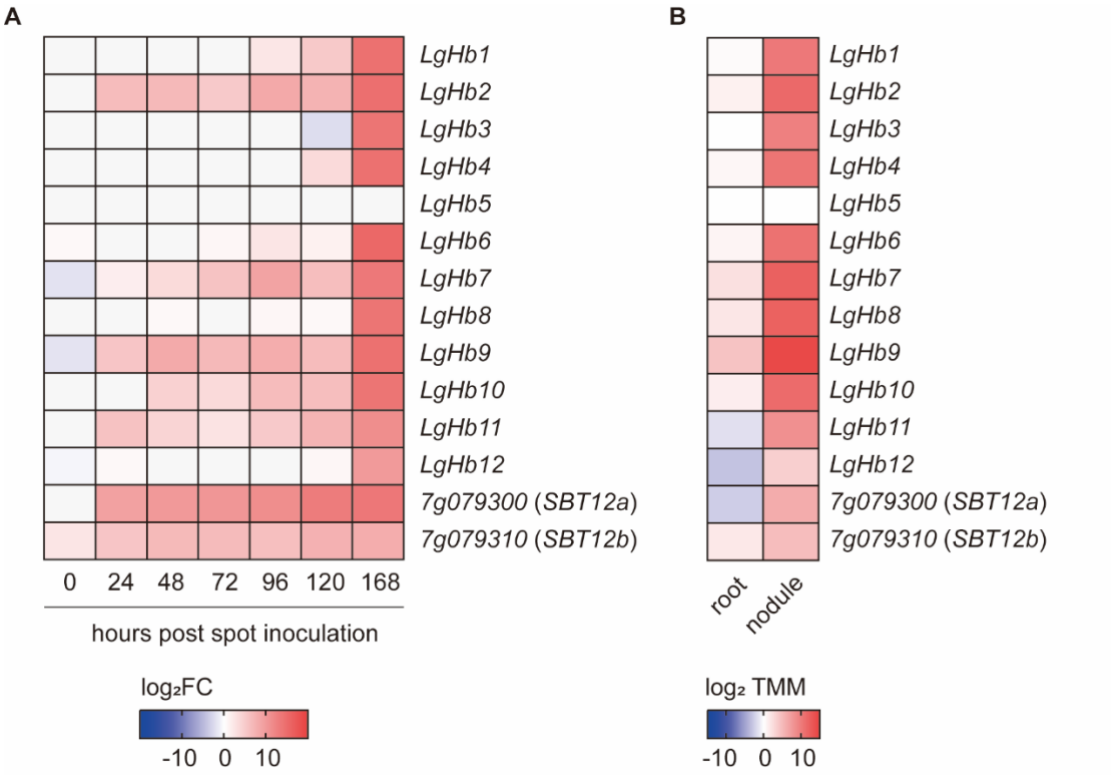


Fig. S1. Expression analyses of the leghemoglobin and subtilase genes in *Medicago truncatula*.

(**A**) Expression heatmap showing the coordinated induction of 12 representative leghemoglobins (LgHbs) (Jiang et al., 2021) and two subtilase (SBT) genes (*Medtr7g079300* and *Medtr7g079310*) during the nodulation process in Medicago (Schiessl et al., 2019). (**B**) Expression comparison of *LgHb* and subtilase genes in nitrogen-starved WT roots and 10-day-old nodule tissues (Roux et al., 2014).

bioRxiv preprint doi: https://doi.org/10.64898/2026.04.09.717438; this version posted April 12, 2026. The copyright holder for this preprint (which was not certified by peer review) is the author/funder, who has granted bioRxiv a license to display the preprint in perpetuity. It is made available under a CC-BY 4.0 International license.

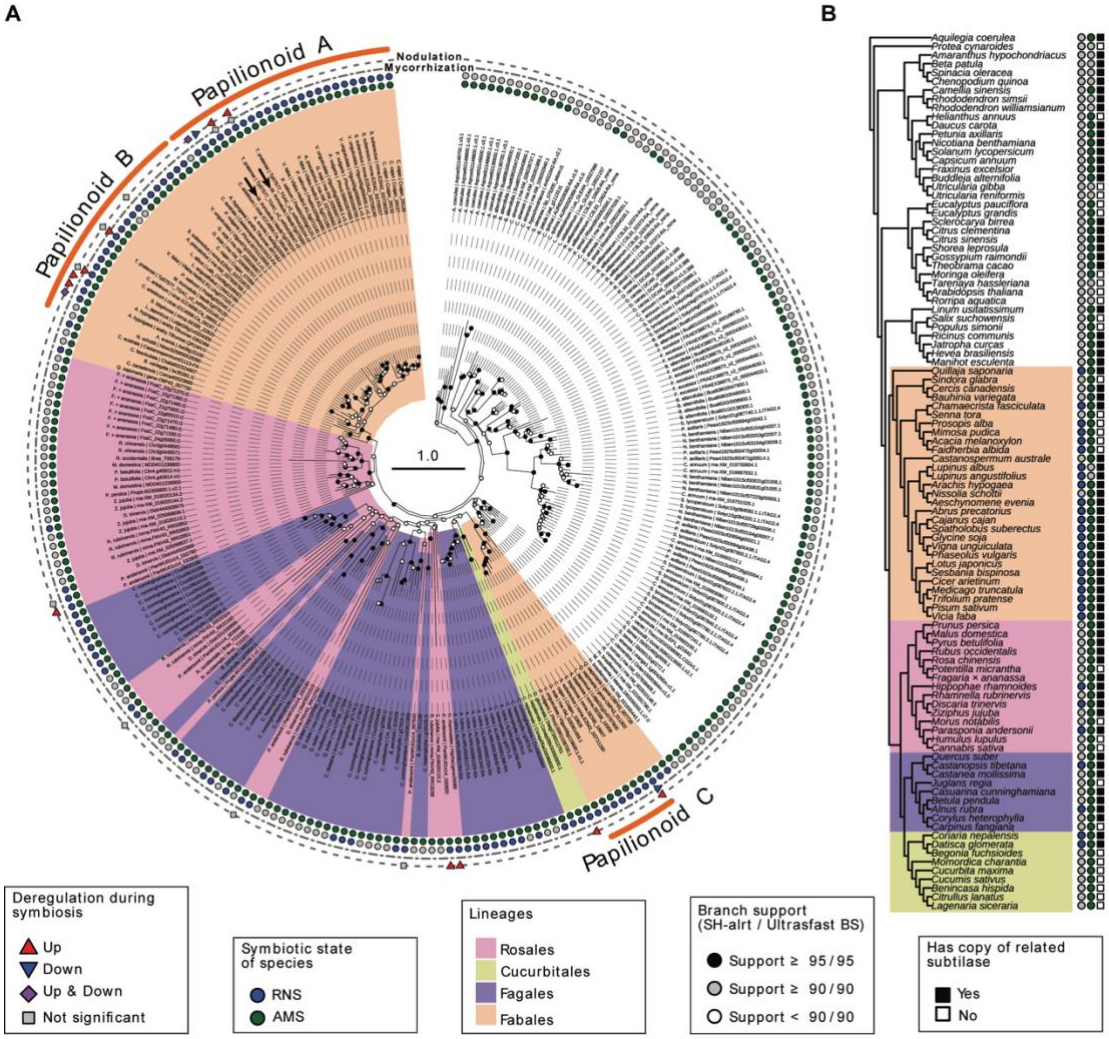


Fig. S2. Phylogenetic analysis of subtilases related to SBT12a and SBT12b and their presence/absence in a variety of eudicots.

(**A**) Phylogenetic tree of subtilases reconstructed with maximum likelihood using the model "Q.plant+C60+F+I+R8". Branch support is shown based on ultrafast bootstrap (% UFBS) and percentage of replicates of the SH-like approximate likelihood ratio test. (**B**) Cladogram of eudicot species included in this analysis, with the presence or absence of the subtilases from (A). Symbiotic state of the species is shown for root nodule symbiosis (RNS; blue) and arbuscular mycorrhizal symbiosis (AMS; green). Genes known to be up- and/or downregulated during RNS or AMS based on the analysis from (A) are marked with a symbol on the outer circle of the tree. The two black arrows indicate the two genes from *M. truncatula* investigated in this study. The scale bar represents the estimated number of substitutions per site.

bioRxiv preprint doi: https://doi.org/10.64898/2026.04.09.717438; this version posted April 12, 2026. The copyright holder for this preprint (which was not certified by peer review) is the author/funder, who has granted bioRxiv a license to display the preprint in perpetuity. It is made available under a CC-BY 4.0 International license.

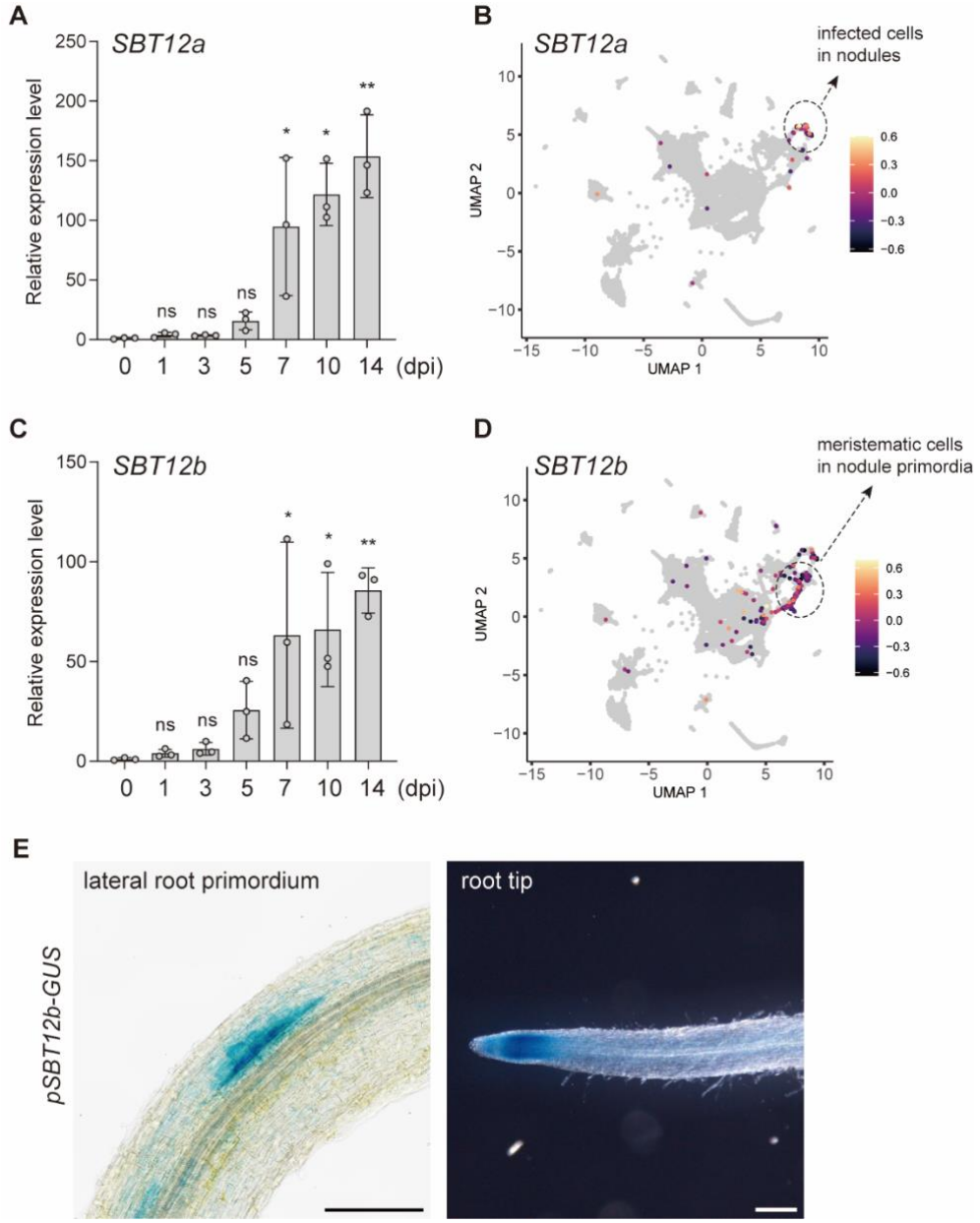


Fig. S3. Expression analysis of *SBT12a* and *SBT12b* during root nodule symbiosis.
(**A** and **C**) qRT-PCR analysis of *SBT12a* (A) and *SBT12b* (C) expression in WT A17 roots inoculated with *S. meliloti 2011*. Root samples were harvested at indicated timepoints. Expression levels were normalized against ubiquitin. Values are the mean of three biological replicates and error bars represent standard deviations. Statistical differences were tested using Kruskal-Wallis test followed by Dunn's multiple comparisons test. * $p<0.05$. ** $p<0.01$. ns represents no significance ($p>0.05$). (**B** and **D**) UMAP projection plots showing expression profiles of *SBT12a* (B) and *SBT12b* (D) across different cell types over the nodulation process (from 0 to 96 hpi). Cells that express *SBT12a* mainly belong to cluster 15, which contains infected cells that eventually become the nitrogen-fixing cells within the nodule. *SBT12b* expression was largely restricted to cells from cluster 9 that is composed of meristematic cells (Pereira et al., 2024). (**E**) Expression of *SBT12b* in lateral root primordium and root tip of inoculated roots, as shown by promoter-GUS assay. Scale bars, 200 µm.

bioRxiv preprint doi: https://doi.org/10.64898/2026.04.09.717438; this version posted April 12, 2026. The copyright holder for this preprint (which was not certified by peer review) is the author/funder, who has granted bioRxiv a license to display the preprint in perpetuity. It is made available under a CC-BY 4.0 International license.

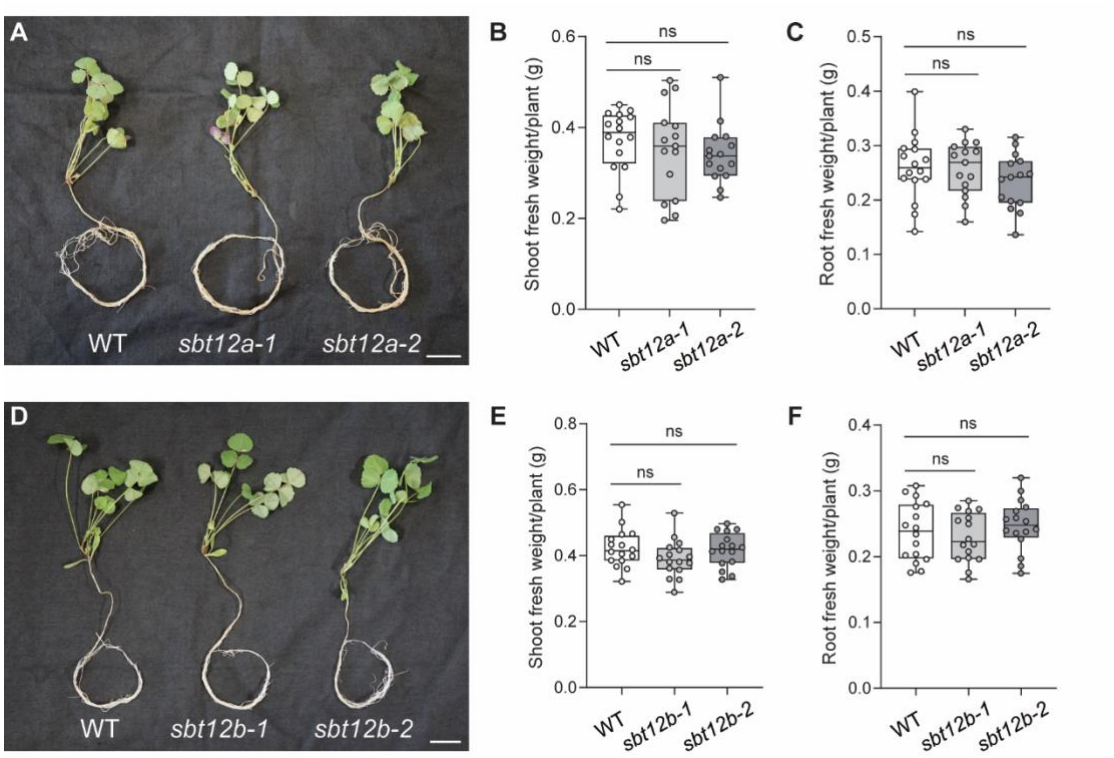


Fig. S4. Phenotypic characterization of *sbt12a* and *sbt12b* mutant lines.
(**A**) 28 days old *sbt12a* mutant seedlings grown in nitrogen-supplied conditions did not exhibit growth phenotypes compared to WT plants. Scale bar, 2 cm. (**B** and **C**) Quantification of shoot (**B**) and root (**C**) fresh weight of *sbt12a* mutant and WT plants from (A). n=16, 15 and 15 for WT, *sbt12a-1* and *sbt12a-2*, respectively. Statistically significant differences were analyzed using Brown-Forsythe and Welch ANOVA test followed by Dunnett's multiple T3 comparisons. ns represents no significance ($p>0.05$). (**D**) 28 days old *sbt12b* mutant plants grown in nitrogen-supplied conditions did not exhibit growth phenotypes compared to WT plants. Scale bar, 2 cm. (**E** and **F**) Quantification of shoot (**E**) and root (**F**) fresh weight of *sbt12b* mutant and WT plants from (D). n=16 for all genotypes. Statistically significant differences were analyzed using Brown-Forsythe and Welch ANOVA test followed by Dunnett's multiple T3 comparisons. ns represents no significance ($p>0.05$).

bioRxiv preprint doi: https://doi.org/10.64898/2026.04.09.717438; this version posted April 12, 2026. The copyright holder for this preprint (which was not certified by peer review) is the author/funder, who has granted bioRxiv a license to display the preprint in perpetuity. It is made available under a CC-BY 4.0 International license.

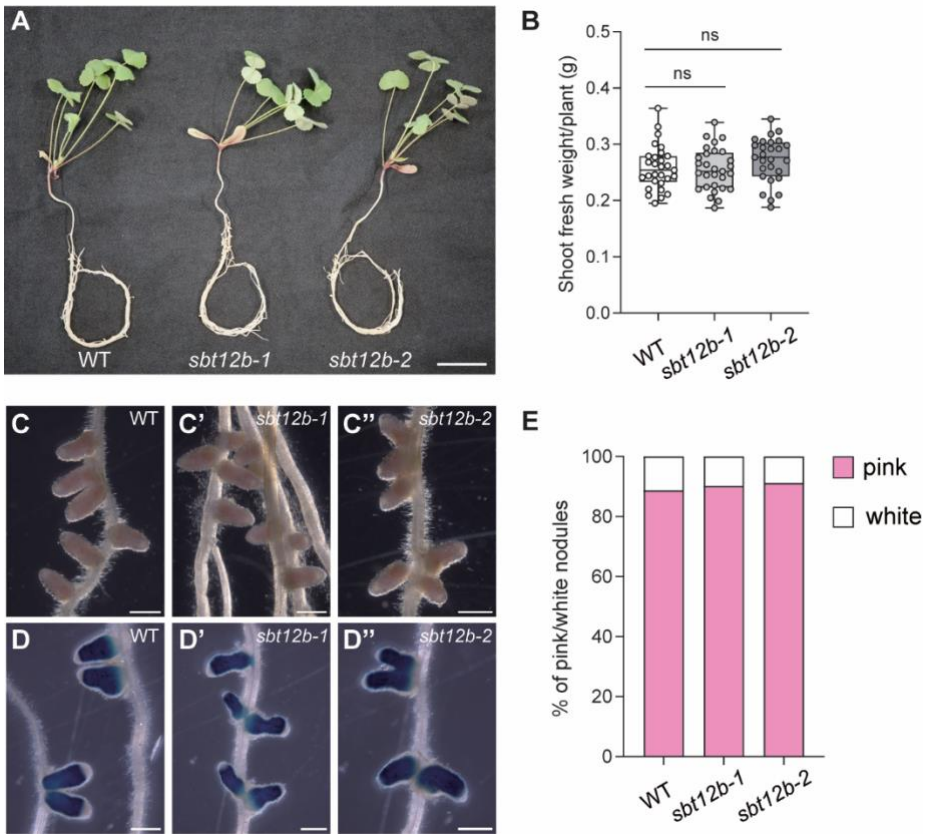


Fig. S5. Phenotypic characterization of *sbt12b* mutants under symbiotic conditions. (**A**) *sbt12b* mutant plants displayed no obvious difference compared to WT at 21 dpi with *S. meliloti 2011*. Scale bar, 2 cm. (**B**) Quantification of shoot fresh weight of *sbt12b* mutant and WT plants at 21 dpi. n=29 for both WT and *sbt12b-1*, and 27 for *sbt12b-2*. Statistically significant differences were analyzed using Brown-Forsythe and Welch ANOVA test followed by Dunnett's multiple T3 comparisons. ns represents no significance ($p>0.05$). (**C** and **D**) Representative nodules formed on WT and *sbt12b* mutant roots at 21 dpi with *S. meliloti 2011 nifH::GUS*. No obvious differences in nodules developing on both *sbt12b* mutants were found in comparison to WT, as shown by the pink color of the nodules indicating that they are completely functional or overall activation of the GUS reporter indicating active nitrogen fixation. Scale bars, 1 mm. (**E**) Ratio of pink and white nodules at 21 dpi. n=29 for both WT and *sbt12b-1*, and 27 for *sbt12b-2*. Nodulation phenotyping was independently repeated three times.

bioRxiv preprint doi: https://doi.org/10.64898/2026.04.09.717438; this version posted April 12, 2026. The copyright holder for this preprint (which was not certified by peer review) is the author/funder, who has granted bioRxiv a license to display the preprint in perpetuity. It is made available under a CC-BY 4.0 International license.

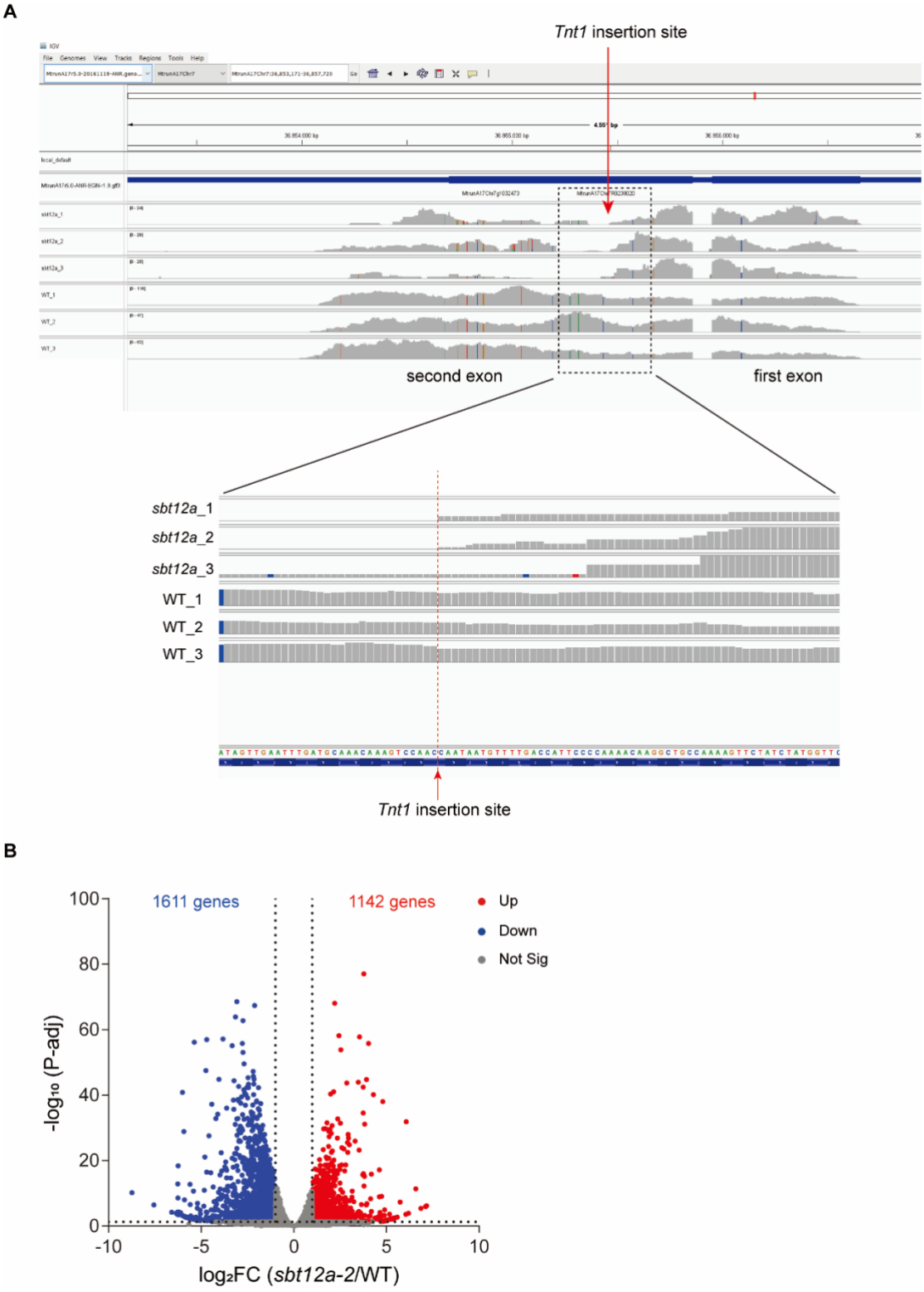


Fig. S6. Transcriptional reprogramming by the *sbt12a* mutation.
(**A**) Distribution of reads mapping to the *SBT12A* gene from RNA-seq analysis. Three biological replicates for both genotypes are shown. Note that for all three *sbt12a-2* nodule samples, reads distribution after *Tnt1* insertion site (indicated by the red arrow) is completely disrupted. (**B**) Volcano plot depicting the distribution of differentially expressed genes (DEGs) comparing *sbt12a-2* and WT nodules. Red and blue circles represent genes that are significantly upregulated (Up) and downregulated (Down) in *sbt12a-2* compared to WT R108, respectively (log_2 fold change >1 and adjusted P-value<0.05). Grey circles represent genes that do not show significant changes (Not Sig) in expression levels.

bioRxiv preprint doi: https://doi.org/10.64898/2026.04.09.717438; this version posted April 12, 2026. The copyright holder for this preprint (which was not certified by peer review) is the author/funder, who has granted bioRxiv a license to display the preprint in perpetuity. It is made available under a CC-BY 4.0 International license.

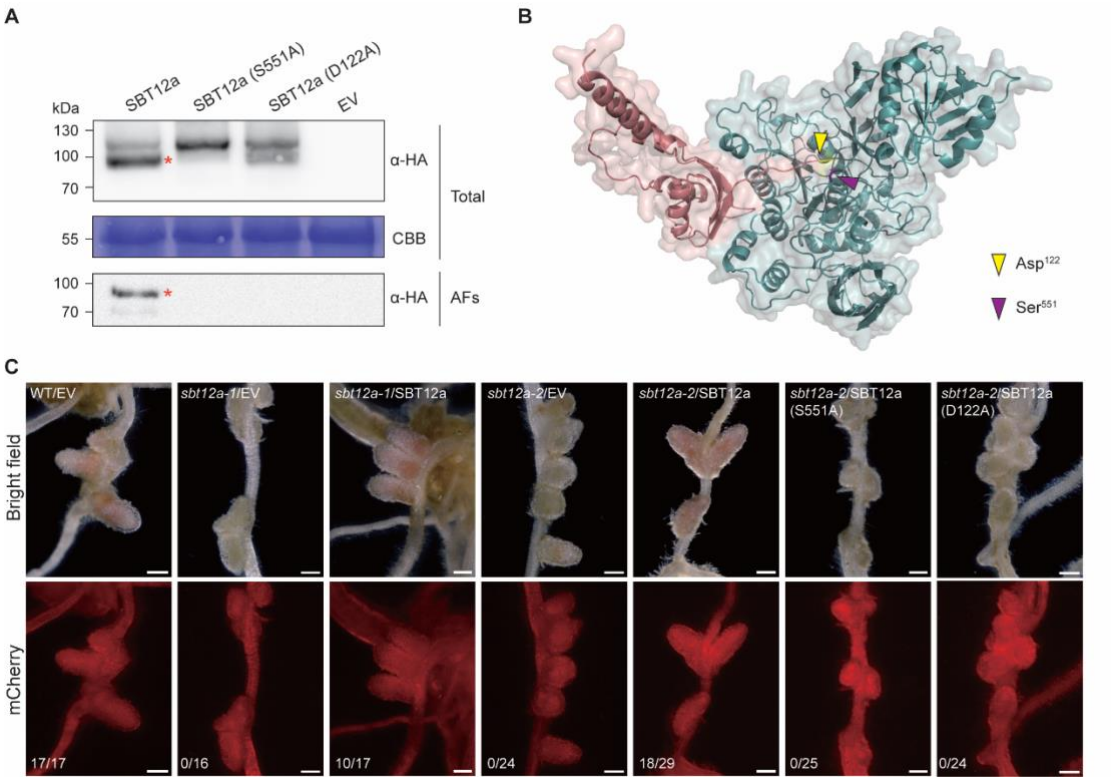


Fig. S7. Characterization of SBT12a as a canonical subtilase.
(**A**) Immunoblot demonstrating the requirement of Ser-551 and Asp-22 for SBT12a self-processing and secretion. WT SBT12a and its mutant variants, S551A and D122A, were fused to the triple hemagglutinin (HA) tag and were transiently expressed in *N. benthamiana* leaves. An empty vector (EV) control was included. Leaf samples were harvested 4 days post agroinfiltration and subsequently subjected to total protein (Total) extraction or apoplastic fluids (AFs) isolation. Coomassie brilliant blue (CBB)-stained Rubisco proteins were used as a loading control. Red asterisks indicate the mature form of SBT12a-3xHA after self-processing. (**B**) Modelled structure of full-length SBT12a protein using AlphaFold3. Signal peptide and prodomain are colored in magenta and mature SBT12a in cyan. The proximity of the prodomain junction Asp-122 and the catalytic site Ser-551, indicated by yellow and purple arrowheads, respectively, suggests the potential self-processing during zymogen maturation. (**C**) Genetic complementation of *sbt12a* mutants. Nodulation defects of *sbt12a* mutants were restored by expressing WT SBT12a, fused with eGFP driven by its native promoter, but not with the mutant variants or the EV. mCherry (red) fused to a nuclear localization signal (NLS) expressed from each construct was used as a selection marker for transformation. Nodule phenotypes were examined at 28 dpi. Fully elongated pink nodules without displaying the sign of premature senescence were considered as complemented nodules. The number of transformed plants having fully elongated pink nodules relative to the total number of transformed plants is shown for each image. Experiments were independently repeated twice with similar results. Scale bars, 500 μm.

bioRxiv preprint doi: https://doi.org/10.64898/2026.04.09.717438; this version posted April 12, 2026. The copyright holder for this preprint (which was not certified by peer review) is the author/funder, who has granted bioRxiv a license to display the preprint in perpetuity. It is made available under a CC-BY 4.0 International license.

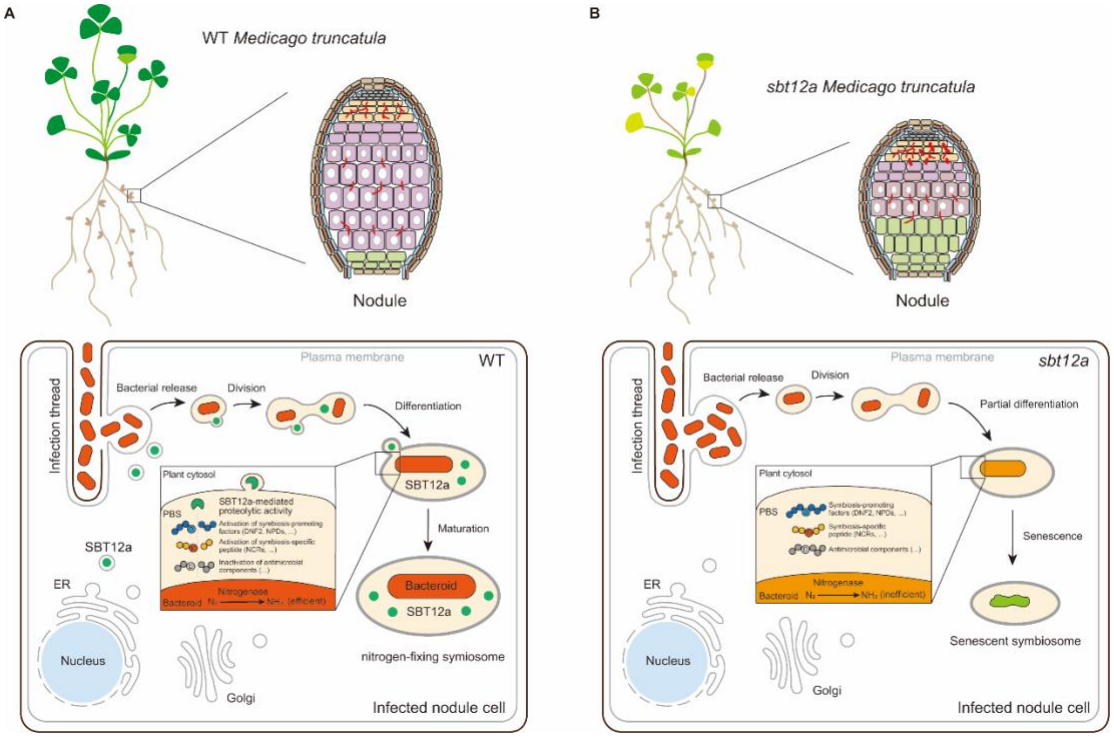


Fig. S8. Proposed working model for SBT12a function.
(**A**) In WT nodules, rhizobia are released from infection threads into nodule cells, and subsequently enclosed within an organelle-like structure called the symbiosome. SBT12a is targeted to the bacterial release sites, where it facilitates this process, and subsequently accumulates in newly formed symbiosomes. Within these symbiosomes, rhizobia proliferate and differentiate into a special form known as bacteroids. This developmental transition is accompanied by the sustained SBT12a-mediated proteolysis in the peribacteroid space. Acting there as a phytaspase with Asp-specific cleavage specificity, SBT12a drives symbiosome stabilization, which is indispensable for sufficient nitrogen fixation occurring in bacteroids. The activity of SBT12a likely involves the activation of symbiosis-promoting regulators, such as DNF2, NPDs and NCR peptides, or the degradation of antimicrobial components. (**B**) In the *sbt12a* mutant, the absence of SBT12a-mediated proteolytic regulation at bacterial release sites and within the peribacteroid space results in altered rhizobial colonization and severe defects in bacteroid differentiation. Consequently, impaired symbiosome maintenance fails to support efficient nitrogen fixation, leading to premature nodule senescence and nitrogen starvation in seedlings.

bioRxiv preprint doi: https://doi.org/10.64898/2026.04.09.717438; this version posted April 12, 2026. The copyright holder for this preprint (which was not certified by peer review) is the author/funder, who has granted bioRxiv a license to display the preprint in perpetuity. It is made available under a CC-BY 4.0 International license.

References

Adema K, Kohlen W, 2024. The symbiosome-a transient organelle in evolution. *J Exp Bot* **75**, 3209-13.

Alunni B, Gourion B, 2016. Terminal bacteroid differentiation in the legume-rhizobium symbiosis: nodule-specific cysteine-rich peptides and beyond. *New Phytol* **211**, 411-7.

Batzenschlager M, Lace B, Zhang N*, et al.*, 2025. Competence for transcellular infection in the root cortex involves a post-replicative, cell-cycle exit decision in Medicago truncatula. *Elife* **12**.

Beloshistov RE, Dreizler K, Galiullina RA*, et al.*, 2018. Phytaspase-mediated precursor processing and maturation of the wound hormone systemin. *New Phytol* **218**, 1167-78.

Berrabah F, Bernal G, Elhosseyn AS*, et al.*, 2023. Insight into the control of nodule immunity and senescence during Medicago truncatula symbiosis. *Plant Physiol* **191**, 729-46.

Berrabah F, Bourcy M, Eschstruth A*, et al.*, 2014. A nonRD receptor-like kinase prevents nodule early senescence and defense-like reactions during symbiosis. *New Phytol* **203**, 1305-14.

Boisson-Dernier A, Chabaud M, Garcia F, Bécard G, Rosenberg C, Barker DG, 2001. Agrobacterium rhizogenes-transformed roots of Medicago truncatula for the study of nitrogen-fixing and endomycorrhizal symbiotic associations. *Mol Plant Microbe Interact* **14**, 695-700.

Bourcy M, Brocard L, Pislariu CI*, et al.*, 2013. Medicago truncatula DNF2 is a PI-PLC-XD-containing protein required for bacteroid persistence and prevention of nodule early senescence and defense-like reactions. *New Phytol* **197**, 1250-61.

Buscaill P, Sanguankiattichai N, Kaschani F*, et al.*, 2024. Subtilase SBT5.2 inactivates flagellin immunogenicity in the plant apoplast. *Nat Commun* **15**, 10431.

Camacho C, Coulouris G, Avagyan V*, et al.*, 2009. BLAST+: architecture and applications. *BMC Bioinformatics* **10**, 421.

Capella-Gutiérrez S, Silla-Martínez JM, Gabaldón T, 2009. trimAl: a tool for automated alignment trimming in large-scale phylogenetic analyses. *Bioinformatics* **25**, 1972-3.

Casaes PA, Ferreira Dos Santos JM, Silva VC*, et al.*, 2024. The radiation of nodulated Chamaecrista species from the rainforest into more diverse habitats has been accompanied by a reduction in growth form and a shift from fixation threads to symbiosomes. *J Exp Bot* **75**, 3643-62.

Catalano CM, Lane WS, Sherrier DJ, 2004. Biochemical characterization of symbiosome membrane proteins from Medicago truncatula root nodules. *Electrophoresis* **25**, 519-31.

Chen C, Buscaill P, Sanguankiattichai N*, et al.*, 2024. Extracellular plant subtilases dampen cold-shock peptide elicitor levels. *Nat Plants* **10**, 1749-60.

De Carvalho-Niebel F, Fournier J, Becker A, Marín Arancibia M, 2024. Cellular insights into legume root infection by rhizobia. *Curr Opin Plant Biol* **81**, 102597.

De Faria SM, Ringelberg JJ, Gross E*, et al.*, 2022. The innovation of the symbiosome has enhanced the evolutionary stability of nitrogen fixation in legumes. *New Phytol* **235**, 2365-77.

bioRxiv preprint doi: https://doi.org/10.64898/2026.04.09.717438; this version posted April 12, 2026. The copyright holder for this preprint (which was not certified by peer review) is the author/funder, who has granted bioRxiv a license to display the preprint in perpetuity. It is made available under a CC-BY 4.0 International license.

Demichev V, Messner CB, Vernardis SI, Lilley KS, Ralser M, 2020. DIA-NN: neural networks and interference correction enable deep proteome coverage in high throughput. *Nat Methods* **17**, 41-4.

Demir F, Kuppusamy M, Perrar A, Huesgen PF, 2022a. Profiling Sequence Specificity of Proteolytic Activities Using Proteome-Derived Peptide Libraries. *Methods Mol Biol* **2447**, 159-74.

Demir F, Niedermaier S, Villamor JG, Huesgen PF, 2018. Quantitative proteomics in plant protease substrate identification. *New Phytol* **218**, 936-43.

Demir F, Perrar A, Mantz M, Huesgen PF, 2022b. Sensitive Plant N-Terminome Profiling with HUNTER. *Methods Mol Biol* **2447**, 139-58.

Deng Z, Yang Y, Marowa P*, et al.*, 2025. Processing of plant peptide signals: critical steps mediated by subtilisins. *Plant Hormones* **1**, e003.

Deutsch EW, Bandeira N, Perez-Riverol Y*, et al.*, 2023. The ProteomeXchange consortium at 10 years: 2023 update. *Nucleic Acids Res* **51**, D1539-d48.

Farkas A, Maróti G, Durgő H*, et al.*, 2014. Medicago truncatula symbiotic peptide NCR247 contributes to bacteroid differentiation through multiple mechanisms. *Proc Natl Acad Sci U S A* **111**, 5183-8.

Fournier J, Imanishi L, Chabaud M*, et al.*, 2018. Cell remodeling and subtilase gene expression in the actinorhizal plant Discaria trinervis highlight host orchestration of intercellular Frankia colonization. *New Phytol* **219**, 1018-30.

Gao F, Yang J, Zhai N*, et al.*, 2023. NCR343 is required to maintain the viability of differentiated bacteroids in nodule cells in Medicago truncatula. *New Phytol* **240**, 815-29.

Gao JP, Jiang S, Su Y*, et al.*, 2022. Intracellular infection by symbiotic bacteria requires the mitotic kinase AURORA1. *Proc Natl Acad Sci U S A* **119**, e2202606119.

Gao JP, Liang W, Liu CW, Xie F, Murray JD, 2024. Unraveling the rhizobial infection thread. *J Exp Bot* **75**, 2235-45.

Gao Y, Chen L, Yang W*, et al.*, 2025. Symbiosome functionality in Medicago truncatula nodules requires continuous clearing of pectins from the symbiosome space. *Nat Commun* **16**, 11118.

Ghantasala S, Roy Choudhury S, 2026. Legume lessons: structural and functional advancements in Nod Factor Receptors for translating root nodule symbiosis. *J Exp Bot* **77**, 890-4.

Guerra-Garcia FJ, Sankari S, 2025. NCR peptides in plant-bacterial symbiosis: applications and importance. *Trends Microbiol* **33**, 147-50.

Guindon S, Dufayard JF, Lefort V, Anisimova M, Hordijk W, Gascuel O, 2010. New algorithms and methods to estimate maximum-likelihood phylogenies: assessing the performance of PhyML 3.0. *Syst Biol* **59**, 307-21.

Harrison MJ, Ivanov S, 2017. Exocytosis for endosymbiosis: membrane trafficking pathways for development of symbiotic membrane compartments. *Curr Opin Plant Biol* **38**, 101-8.

Horváth B, Domonkos Á, Kereszt A*, et al.*, 2015. Loss of the nodule-specific cysteine rich peptide, NCR169, abolishes symbiotic nitrogen fixation in the Medicago truncatula dnf7 mutant. *Proc Natl Acad Sci U S A* **112**, 15232-7.

Horváth B, Güngör B, Tóth M*, et al.*, 2023. The Medicago truncatula nodule-specific cysteine-rich peptides, NCR343 and NCR-new35 are required for the maintenance of rhizobia in nitrogen-fixing nodules. *New Phytol* **239**, 1974-88.

Huisman R, Geurts R, 2020. A Roadmap toward Engineered Nitrogen-Fixing Nodule Symbiosis. *Plant Commun* **1**, 100019.

bioRxiv preprint doi: https://doi.org/10.64898/2026.04.09.717438; this version posted April 12, 2026. The copyright holder for this preprint (which was not certified by peer review) is the author/funder, who has granted bioRxiv a license to display the preprint in perpetuity. It is made available under a CC-BY 4.0 International license.

Jhu MY, Oldroyd GED, 2023. Dancing to a different tune, can we switch from chemical to biological nitrogen fixation for sustainable food security? *PLoS Biol* **21**, e3001982.

Jiang S, Jardinaud MF, Gao J*, et al.*, 2021. NIN-like protein transcription factors regulate leghemoglobin genes in legume nodules. *Science* **374**, 625-8.

Kalyaanamoorthy S, Minh BQ, Wong TKF, Von Haeseler A, Jermiin LS, 2017. ModelFinder: fast model selection for accurate phylogenetic estimates. *Nat Methods* **14**, 587-9.

Katoh K, Standley DM, 2013. MAFFT multiple sequence alignment software version 7: improvements in performance and usability. *Mol Biol Evol* **30**, 772-80.

Kim M, Chen Y, Xi J, Waters C, Chen R, Wang D, 2015. An antimicrobial peptide essential for bacterial survival in the nitrogen-fixing symbiosis. *Proc Natl Acad Sci U S A* **112**, 15238-43.

Kistner C, Winzer T, Pitzschke A*, et al.*, 2005. Seven Lotus japonicus genes required for transcriptional reprogramming of the root during fungal and bacterial symbiosis. *Plant Cell* **17**, 2217-29.

Lace B, Su C, Invernot Perez D*, et al.*, 2023. RPG acts as a central determinant for infectosome formation and cellular polarization during intracellular rhizobial infections. *Elife* **12**.

Laplaze L, Ribeiro A, Franche C*, et al.*, 2000. Characterization of a Casuarina glauca nodule-specific subtilisin-like protease gene, a homolog of Alnus glutinosa ag12. *Mol Plant Microbe Interact* **13**, 113-7.

Lee T, Orvosova M, Batzenschlager M*, et al.*, 2024. Light-sensitive short hypocotyl genes confer symbiotic nodule identity in the legume Medicago truncatula. *Curr Biol* **34**, 825-40.e7.

Lefebvre B, Timmers T, Mbengue M*, et al.*, 2010. A remorin protein interacts with symbiotic receptors and regulates bacterial infection. *Proc Natl Acad Sci U S A* **107**, 2343-8.

Li Z, Sheerin DJ, Von Roepenack-Lahaye E, Stahl M, Hiltbrunner A, 2022. The phytochrome interacting proteins ERF55 and ERF58 repress light-induced seed germination in Arabidopsis thaliana. *Nat Commun* **13**, 1656.

Liang P, Schmitz C, Lace B*, et al.*, 2021. Formin-mediated bridging of cell wall, plasma membrane, and cytoskeleton in symbiotic infections of Medicago truncatula. *Curr Biol* **31**, 2712-9.e5.

Liang P, Stratil TF, Popp C*, et al.*, 2018. Symbiotic root infections in Medicago truncatula require remorin-mediated receptor stabilization in membrane nanodomains. *Proc Natl Acad Sci U S A* **115**, 5289-94.

Libourel C, Keller J, Brichet L*, et al.*, 2023. Comparative phylotranscriptomics reveals ancestral and derived root nodule symbiosis programmes. *Nat Plants* **9**, 1067-80.

Meyer M, Leptihn S, Welz M, Schaller A, 2016. Functional Characterization of Propeptides in Plant Subtilases as Intramolecular Chaperones and Inhibitors of the Mature Protease. *J Biol Chem* **291**, 19449-61.

Minh BQ, Dang CC, Vinh LS, Lanfear R, 2021. QMaker: Fast and Accurate Method to Estimate Empirical Models of Protein Evolution. *Syst Biol* **70**, 1046-60.

Minh BQ, Nguyen MA, Von Haeseler A, 2013. Ultrafast approximation for phylogenetic bootstrap. *Mol Biol Evol* **30**, 1188-95.

bioRxiv preprint doi: https://doi.org/10.64898/2026.04.09.717438; this version posted April 12, 2026. The copyright holder for this preprint (which was not certified by peer review) is the author/funder, who has granted bioRxiv a license to display the preprint in perpetuity. It is made available under a CC-BY 4.0 International license.

Minh BQ, Schmidt HA, Chernomor O*, et al.*, 2020. IQ-TREE 2: New Models and Efficient Methods for Phylogenetic Inference in the Genomic Era. *Mol Biol Evol* **37**, 1530-4.

Nakagawa M, Ueyama M, Tsuruta H*, et al.*, 2010. Functional analysis of the cucumisin propeptide as a potent inhibitor of its mature enzyme. *J Biol Chem* **285**, 29797-807.

Paradis E, Schliep K, 2019. ape 5.0: an environment for modern phylogenetics and evolutionary analyses in R. *Bioinformatics* **35**, 526-8.

Pereira WJ, Boyd J, Conde D*, et al.*, 2024. The single-cell transcriptome program of nodule development cellular lineages in Medicago truncatula. *Cell Rep* **43**, 113747.

Perez-Riverol Y, Bandla C, Kundu DJ*, et al.*, 2025. The PRIDE database at 20 years: 2025 update. *Nucleic Acids Res* **53**, D543-d53.

Pierre O, Hopkins J, Combier M*, et al.*, 2014. Involvement of papain and legumain proteinase in the senescence process of Medicago truncatula nodules. *New Phytol* **202**, 849-63.

Pislariu CI, Sinharoy S, Torres-Jerez I, Nakashima J, Blancaflor EB, Udvardi MK, 2019. The Nodule-Specific PLAT Domain Protein NPD1 Is Required for Nitrogen-Fixing Symbiosis. *Plant Physiol* **180**, 1480-97.

Price MN, Dehal PS, Arkin AP, 2010. FastTree 2--approximately maximum-likelihood trees for large alignments. *PLoS One* **5**, e9490.

Qiao L, Sun H, Tang J*, et al.*, 2026. Nanodomain-localized formin gates symbiotic microbial entry in legume and solanaceous plants. *Science* **391**, 1036-45.

Quang Le S, Gascuel O, Lartillot N, 2008. Empirical profile mixture models for phylogenetic reconstruction. *Bioinformatics* **24**, 2317-23.

Rappsilber J, Mann M, Ishihama Y, 2007. Protocol for micro-purification, enrichment, pre-fractionation and storage of peptides for proteomics using StageTips. *Nat Protoc* **2**, 1896-906.

Reichardt S, Piepho HP, Stintzi A, Schaller A, 2020. Peptide signaling for drought-induced tomato flower drop. *Science* **367**, 1482-5.

Reichardt S, Repper D, Tuzhikov AI*, et al.*, 2018. The tomato subtilase family includes several cell death-related proteinases with caspase specificity. *Sci Rep* **8**, 10531.

Ren J, Wang Q, Zhang X*, et al.*, 2025. Control of Rhizobia Endosymbiosis by Coupling ER Expansion with Enhanced UPR. *Advanced Science*.

Revell LJ, 2024. phytools 2.0: an updated R ecosystem for phylogenetic comparative methods (and other things). *PeerJ* **12**, e16505.

Ritchie ME, Phipson B, Wu D*, et al.*, 2015. limma powers differential expression analyses for RNA-sequencing and microarray studies. *Nucleic Acids Res* **43**, e47.

Roux B, Rodde N, Jardinaud MF*, et al.*, 2014. An integrated analysis of plant and bacterial gene expression in symbiotic root nodules using laser-capture microdissection coupled to RNA sequencing. *Plant J* **77**, 817-37.

Ruan Y, Dong S, Jiang S*, et al.*, 2026. The molecular basis of the binding and specific activation of rhizobial NodD by flavonoids. *Science* **391**, 184-9.

Rübsam H, Krönauer C, Abel NB*, et al.*, 2023. Nanobody-driven signaling reveals the core receptor complex in root nodule symbiosis. *Science* **379**, 272-7.

bioRxiv preprint doi: https://doi.org/10.64898/2026.04.09.717438; this version posted April 12, 2026. The copyright holder for this preprint (which was not certified by peer review) is the author/funder, who has granted bioRxiv a license to display the preprint in perpetuity. It is made available under a CC-BY 4.0 International license.

Schaller A, Stintzi A, Rivas S, *et al.*, 2018. From structure to function - a family portrait of plant subtilases. *New Phytol* **218**, 901-15.

Schiessl K, Lilley JLS, Lee T, *et al.*, 2019. NODULE INCEPTION Recruits the Lateral Root Developmental Program for Symbiotic Nodule Organogenesis in Medicago truncatula. *Curr Biol* **29**, 3657-68.e5.

Schilling O, Overall CM, 2008. Proteome-derived, database-searchable peptide libraries for identifying protease cleavage sites. *Nat Biotechnol* **26**, 685-94.

Sénéchal F, Graff L, Surcouf O, *et al.*, 2014. Arabidopsis PECTIN METHYLESTERASE17 is co-expressed with and processed by SBT3.5, a subtilisin-like serine protease. *Ann Bot* **114**, 1161-75.

Sinharoy S, Torres-Jerez I, Bandyopadhyay K, *et al.*, 2013. The C2H2 transcription factor regulator of symbiosome differentiation represses transcription of the secretory pathway gene VAMP721a and promotes symbiosome development in Medicago truncatula. *Plant Cell* **25**, 3584-601.

Stockert F, Baeta H, Huesgen PF, 2024. Analysis of mitochondrial targeting signal cleavage and protein processing by mass spectrometry. *Methods Enzymol* **706**, 215-42.

Su C, Zhang G, Rodriguez-Franco M, *et al.*, 2023. Transcellular progression of infection threads in Medicago truncatula roots is associated with locally confined cell wall modifications. *Curr Biol* **33**, 533-42.e5.

Svistoonoff S, Laplaze L, Auguy F, *et al.*, 2003. cg12 expression is specifically linked to infection of root hairs and cortical cells during Casuarina glauca and Allocasuarina verticillata actinorhizal nodule development. *Mol Plant Microbe Interact* **16**, 600-7.

Tadege M, Wen J, He J, *et al.*, 2008. Large-scale insertional mutagenesis using the Tnt1 retrotransposon in the model legume Medicago truncatula. *Plant J* **54**, 335-47.

Takeda N, Haage K, Sato S, Tabata S, Parniske M, 2011. Activation of a Lotus japonicus subtilase gene during arbuscular mycorrhiza is dependent on the common symbiosis genes and two cis-active promoter regions. *Mol Plant Microbe Interact* **24**, 662-70.

Takeda N, Sato S, Asamizu E, Tabata S, Parniske M, 2009. Apoplastic plant subtilases support arbuscular mycorrhiza development in Lotus japonicus. *Plant J* **58**, 766-77.

Taylor A, Qiu YL, 2017. Evolutionary History of Subtilases in Land Plants and Their Involvement in Symbiotic Interactions. *Mol Plant Microbe Interact* **30**, 489-501.

Team RC, 2022. R: A Language and Environment for Statistical Computing (Version 4.2.0) [Computer software].

Trujillo DI, Silverstein KaT, Young ND, 2019. Nodule-specific PLAT domain proteins are expanded in the Medicago lineage and required for nodulation. *New Phytol* **222**, 1538-50.

Van De Velde W, Zehirov G, Szatmari A, *et al.*, 2010. Plant peptides govern terminal differentiation of bacteria in symbiosis. *Science* **327**, 1122-6.

Wang C, Yu H, Luo L, *et al.*, 2016. NODULES WITH ACTIVATED DEFENSE 1 is required for maintenance of rhizobial endosymbiosis in Medicago truncatula. *New Phytol* **212**, 176-91.

Wang D, Griffitts J, Starker C, *et al.*, 2010. A nodule-specific protein secretory pathway required for nitrogen-fixing symbiosis. *Science* **327**, 1126-9.

bioRxiv preprint doi: https://doi.org/10.64898/2026.04.09.717438; this version posted April 12, 2026. The copyright holder for this preprint (which was not certified by peer review) is the author/funder, who has granted bioRxiv a license to display the preprint in perpetuity. It is made available under a CC-BY 4.0 International license.

Weber E, Engler C, Gruetzner R, Werner S, Marillonnet S, 2011. A modular cloning system for standardized assembly of multigene constructs. *PLoS One* **6**, e16765.

Weng SSH, Demir F, Ergin EK*, et al.*, 2019. Sensitive Determination of Proteolytic Proteoforms in Limited Microscale Proteome Samples. *Mol Cell Proteomics* **18**, 2335-47.

Xiao TT, Schilderink S, Moling S*, et al.*, 2014. Fate map of Medicago truncatula root nodules. *Development* **141**, 3517-28.

Yang J, Zhai N, Chen Y, Wang L, Chen R, Pan H, 2023. A signal peptide peptidase is required for ER-symbiosome proximal association and protein secretion. *Nat Commun* **14**, 4355.

Yu F, Teo GC, Kong AT*, et al.*, 2023. Analysis of DIA proteomics data using MSFragger-DIA and FragPipe computational platform. *Nat Commun* **14**, 4154.

Yu G, Smith D, Zhu H, Guan Y, Lam T, 2016. ggtree : an R package for visualization and annotation of phylogenetic trees with their covariates and other associated data. *Methods in Ecology and Evolution* **8**.

Yun J, Wang C, Zhang F*, et al.*, 2023. A nitrogen fixing symbiosis-specific pathway required for legume flowering. *Sci Adv* **9**, eade1150.

Zhang G, Ott T, 2024. Cellular morphodynamics and signaling around the transcellular passage cleft during rhizobial infections of legume roots. *Curr Opin Cell Biol* **91**, 102436.

Zhang R, Shen Y, He J*, et al.*, 2023. Nodule-specific cysteine-rich peptide 343 is required for symbiotic nitrogen fixation in Medicago truncatula. *Plant Physiol* **193**, 1897-912.

Zhang X, Wang Q, Wu J*, et al.*, 2022. A legume kinesin controls vacuole morphogenesis for rhizobia endosymbiosis. *Nat Plants* **8**, 1275-88.

Zhang X, Wu J, Kong Z, 2024. Cellular basis of legume-rhizobium symbiosis. *Plant Commun* **5**, 101045.

Zhao L, Ji CY, Murray JD, Liu CW, 2025. A legume cellulase required for rhizobial infection and colonization in root nodule symbiosis. *Nat Commun* **16**, 6663.